

STIS Echelle Observations of the Seyfert Galaxy NGC 4151: Physical Conditions in the Ultraviolet Absorbers¹

S. B. Kraemer², D. M. Crenshaw², J. B. Hutchings³, I.M. George^{4,5}, A.C. Danks⁶, T.R. Gull⁷, M.E. Kaiser⁸, C.H. Nelson⁹, & D. Weistrop⁹

ABSTRACT

We have examined the physical conditions in intrinsic UV-absorbing gas in the Seyfert galaxy NGC 4151, using echelle spectra obtained with the Space Telescope Imaging Spectrograph (STIS) on the *Hubble Space Telescope (HST)* on 1999 July 19. We confirm the presence of the kinematic components detected in earlier Goddard High Resolution Spectrograph (GHRS) observations, all of which appear to be outflowing from the nucleus, as well as a new broad absorption feature at a radial velocity of -1680 km s^{-1} . The UV continuum of NGC 4151 was a factor of about 4 lower than in observations taken over the previous two

¹Based on observations made with the NASA/ESA Hubble Space Telescope. STScI is operated by the Association of Universities for Research in Astronomy, Inc. under the NASA contract NAS5-26555.

²Catholic University of America, NASA's Goddard Space Flight Center, Code 681, Greenbelt, MD 20771; stiskraemer@yancey.gsfc.nasa.gov, crenshaw@buckeye.gsfc.nasa.gov.

³Dominion Astrophysical Observatory, National Research Council of Canada, Victoria, BC V8X 4M6, Canada; John.Hutchings@hia.nrc.ca.

⁴Laboratory for High Energy Astrophysics, NASA's Goddard Space Flight Center, Code 662, Greenbelt, MD 20771; george@oberon.gsfc.nasa.gov

⁵Joint Center for Astrophysics, University of Maryland, Baltimore County, 1000 Hilltop Circle, Baltimore, MD 21250

⁶Raytheon Polar Services, NASA's Goddard Space Flight Center, Code 681, Greenbelt, MD 20771; danks@stars.gsfc.nasa.gov.

⁷NASA's Goddard Space Flight Center, Code 681, Greenbelt, MD 20771; gull@sea.gsfc.nasa.gov.

⁸Department of Physics and Astronomy, Johns Hopkins University, 3400 North Charles Street, Baltimore, MD 21218; kaiser@munin.pha.jhu.edu.

⁹Department of Physics, University of Nevada, Las Vegas, 4505 Maryland Parkway, Las Vegas, NV 89154-4002; cnelson@physics.unlv.edu, weistrop@nevada.edu.

years, and we argue the changes in the column density of the low ionization absorption lines associated with the broad component at -490 km s^{-1} reflect the decrease in the ionizing flux. Most of the strong absorption lines (e.g., N V, C IV, Si IV, etc.) from this component are saturated, but show substantial residual flux in their cores, indicating that the absorber does not fully cover the source of emission. Our interpretation is that the unocculted light is due to scattering by free electrons from an extended region, which reflects continuum, emission lines, and absorption lines. For the first time in such a study, we have been able to constrain the densities for this kinematic component and several others based on the strength of absorption lines from metastable states of C III and Fe II, and/or the ratios of ground and fine structure lines of O I, C II, and Si II. We have generated a set of photoionization models which not only successfully match the ionic column densities for each component during the present low flux state, but also those seen in previous high flux states with the GHRS and STIS, confirming that the absorbers are photoionized and respond to the changes in the continuum flux. Based on the model parameters (ionization parameter and density), we have been able to map the relative radial positions of the absorbers. We find that the absorbing gas decreases in density with distance. Finally, none of the UV absorbers is of sufficiently large column density or high enough ionization state to account for the observed X-ray absorption, while the scatterer is too highly ionized. Hence, the X-ray absorption must arise in a separate component of circumnuclear gas.

Subject headings: galaxies: individual (NGC 4151) – galaxies: Seyfert - ultraviolet: galaxies

1. Introduction

NGC 4151 ($cz = 995 \text{ km s}^{-1}$; determined from 21 cm observations, de Vaucouleurs et al. [1991]) is the first Seyfert galaxy known to show intrinsic absorption that could be attributed to the active nucleus. Ultraviolet observations of NGC 4151 by the *IUE* (Boksenberg et al. 1978) and subsequent far-ultraviolet observations by the *Hopkins Ultraviolet Telescope* (*HUT*, Kriss et al. 1992) revealed a number of absorption lines from species that span a wide range in ionization potential (e.g., O I to O VI), as well as fine-structure and metastable absorption lines. The intrinsic UV absorption was found to be variable in ionic column density, but no variations in radial velocities were detected (Bromage et al. 1985). The ionization state of the UV absorbers are generally well correlated with the UV continuum

flux level; the equivalent widths of low ionization species are negatively correlated with the flux level, while the those of the high ionization species are positively correlated (Bromage et al. 1985). More recent observations of NGC 4151 were obtained with the Goddard High Resolution Spectrograph (GHRS) at high spectral resolution ($\sim 15 \text{ km s}^{-1}$) over limited wavelength regions by Weymann et al. (1997). The GHRS spectra revealed that the C IV and Mg II absorption lines, detected in six major kinematic components, were remarkably stable over the time period 1992 – 1996, with the notable exception of a transient feature which appeared on the blue wing of the broad C IV emission. However, this feature, which was discussed in our previous paper (Crenshaw et al. 2000b; hereafter Paper I), turns out to be due to Si II, rather than a high velocity C IV component, as suggested by Weymann et al. (1997),

X-ray spectra of NGC 4151 reveal the presence of a large intrinsic column of atomic gas (see, e.g., Barr et al. 1977; Holt et al. 1980). Based on *ASCA* spectra (see George et al. 1998, and references therein), the 0.6 – 10 keV continuum of NGC 4151 can be fit as a flat power law ($\alpha = 0.3 - 0.7$), with an absorber of column density $N_H \sim 10^{22-23} \text{ cm}^{-2}$, which is most likely ionized, as suggested by Yaqoob, Warwick, & Pounds (1989). NGC 4151 is highly variable in X-rays (cf. Perola et al. 1982, 1986), and the X-ray absorber appears to respond to changes in the 2 – 10 keV flux, although the changes in total column and ionization state are not simply correlated with the X-ray luminosity (George et al. 1998). For example, Weaver et al. (1994) found evidence that the ionization state and column density of the absorber were both higher when the source was fainter, which may be more easily explained by transverse motion.

In the Hubble Space Telescope (*HST*) survey of intrinsic UV absorption lines in Seyfert galaxies by Crenshaw et al. (1999), NGC 4151 stood out as an unusual object. Of the ten Seyfert galaxies in this sample with intrinsic absorption, all showed C IV and N V absorption, but only NGC 4151 showed Mg II absorption (although, recently, the presence of Mg II absorption has been confirmed in the Seyfert 1 galaxy NGC 3227; Kraemer et al. 2000b). NGC 4151 is also unusual in the sense that it is the only active galaxy known to show metastable C III* $\lambda 1175$ absorption, which is indicative of relatively high electron densities ($\sim 10^9 \text{ cm}^{-3}$, Bromage et al. 1985).

We obtained STIS echelle spectra of the UV spectrum to study the intrinsic absorption in detail. These observations are part of a long-term project on NGC 4151 by members of the Instrument Definition Team (IDT) of the Space Telescope Imaging Spectrograph (STIS) on *HST*. In Paper I, we concentrated on the variability of the absorption features in the spectral region surrounding the broad C IV emission. In this paper, we present results on the entire UV spectrum and the kinematics and physical conditions in the intrinsic absorbers.

2. Observational Results

We observed the nucleus of NGC 4151 with a $0''.2 \times 0''.2$ aperture and the STIS E140M and E230M gratings to obtain a spectral coverage of 1150 – 3100 Å at a velocity resolution of 7 – 10 km s⁻¹ (the “STIS2” dataset). In Paper I, we give the details of the STIS observations and the data reduction procedures. We obtained the STIS echelle spectra on 1999 July 19, when the continuum and broad emission lines were in a low state compared to previous STIS and GHRS observations. We found that the UV continuum decreased by a factor of ~ 4 over the previous two years, which resulted in a dramatic increase in the column densities of the broad components of the low-ionization absorption lines (e.g., Si II, Fe II, and Al II). In addition to the absorption lines seen in *IUE* spectra during previous low states (Bromage et al. 1985), we identified numerous broad Fe II absorption lines that arise from metastable levels as high as 4.6 eV above the ground state. We concluded that the low-ionization absorption lines are very sensitive to changes in the ionizing continuum, and that the extreme variability in these lines could explain a couple of puzzling aspects of the UV spectrum of NGC 4151: the “transient absorption feature” in the blue wing of the C IV emission feature (Weymann et al. 1997) and the “satellite emission lines” (Ulrich et al. 1985; Clavel et al. 1987).

2.1. Line Identification

Figure 1 (a – f) shows the STIS echelle spectra over the entire UV bandpass. The broad absorption features (FWHM = 435 km s⁻¹) appear at a heliocentric redshift of 0.0017 (velocity centroid = -490 km s⁻¹ with respect to the nucleus), and correspond to a blend of kinematic components D and E in Weymann et al. (1997). We give our line identifications of the broad absorption features above the spectrum shown in Figure 1. Most of the line identifications at the top of Figure 1 agree with those claimed in *IUE* high-dispersion spectra by Bromage et al. (1985), including numerous resonance lines, excited fine-structure lines of C II, O I, and Si II, and the metastable C III* $\lambda 1175$ blend. In addition we have firm identifications of Ni II lines with oscillator strengths $f > 0.04$ (Morton, York, & Jenkins 1988). Broad Cr II and Mn II absorption may also be present, but these identifications are less certain and may be affected by the numerous Fe II absorption lines in the spectra (see below). We find no evidence in the STIS spectra for the metastable He II $\lambda 1640$ and metastable He I $\lambda 2764$, $\lambda 2829$, and $\lambda 2945$ lines claimed by Bromage et al. (1985), although the Fe II lines may be masking these features as well.

Below the STIS echelle spectra in Figure 1, we plot all of the Fe II UV lines in the lists of Silvis & Bruhweiler (2000), which include multiplets from levels as high as 4.6 eV above

the ground state. Few regions in the spectra are unaffected by Fe II absorption; this can be seen by noting that local regions of the spectra with no Fe II multiplets plotted below them (and no other absorption features above) are much higher than surrounding regions (e.g., 1341 – 1346 Å, 1593 – 1602 Å, 2648 – 2662 Å, 3014 – 3044 Å). It is also clear that multiplets from levels high above the ground state must contribute; for example, Fe II UV multiplet HU, arising from a level 4.1 eV above ground, is clearly present in the observed spectrum at 1310 – 1314 Å (although the shorter wavelength lines are blended with Si II* λ 1309.3)

The narrow kinematic components of absorption identified by Weymann et al. (1997) are also seen in a number of ionic species. Figure 2 demonstrates this point with plots of the Si IV λ 1393.8 and S II λ 1253.8 absorption as a function of radial velocity (with respect to the systemic redshift of 0.00332). For the relatively high ionization line of Si IV, components A, B (Galactic), C, D+E (the broad feature), F, and F' are evident (F and F' likely arise in the interstellar medium or halo of NGC 4151, Weymann et al. 1997). For the low ionization line of S II, components B, D+E, E', and F are present (E' is not seen in the high ionization lines). The presence or absence of kinematic components in different ions provide valuable information on the physical conditions in each component, which will be explored in this paper. An expanded atlas of the STIS echelle spectra with our identification of each component of absorption is given in Danks et al. (2000).

2.2. Saturation and Scattered Light

There are a number of Galactic (component B) lines that are heavily saturated (e.g., Si III λ 1206.5, Si II λ 1260.4, C II λ 1334.5, Mg II $\lambda\lambda$ 2796.3, 2803.5), as evidenced by their extremely small residual intensities. The troughs of these Galactic features all lie within 1% of the nearby continuum flux levels, indicating not only heavy saturation, but accurate subtraction of the instrumental scattered light as well (see Paper I). Although the residual intensities in the troughs of the broad (D+E) absorption lines are much higher (>7% of the continuum in all cases), several clues indicate that most of the broad absorption lines are actually highly saturated, and the large residual intensities are due to unabsorbed (e.g., scattered) light in NGC 4151.

Calculation of the covering factor in the line of sight using the doublet method (Hamann et al. 1997; Crenshaw et al. 1999) yields values significantly less than unity in the troughs: 0.91 ± 0.02 for N V $\lambda\lambda$ 1238.8, 1242.8 and C IV $\lambda\lambda$ 1548.2, 1550.8; 0.85 ± 0.02 for Si IV $\lambda\lambda$ 1393.8, 1402.8; and 0.62 ± 0.04 for Mg II $\lambda\lambda$ 2796.3, 2803.5. This indicates unabsorbed emission in the troughs that is not constant as a function of wavelength. In addition, the presence of a number of Fe II lines with small *gf* values (Silvas & Bruhweiler 2000), indicates

that Fe II lines with much higher values must be saturated. For example, in the 2900 – 3100 Å region in Figure 1f, the Fe II lines in multiplet 78 with moderate gf values are nearly the same strength as the line with the largest value (at 2990 Å), and even the line with the lowest gf value in this multiplet is relatively strong. Lines in other multiplets with much higher gf values are clearly saturated, although the residual intensities in their troughs can be quite large. Finally, the strengths of broad absorption lines with low oscillator strengths and/or low abundances (e.g., S II, Ni II) indicate that many of the other low-ionization absorption lines should be saturated. Thus we have strong evidence for heavy saturation of the D+E component in most of the absorption lines and a significant amount of UV light in the nucleus that is not occulted by these broad absorbers.

There are indications that the spectrum of the unocculted light is not simple (e.g., a power-law continuum). A power-law continuum drawn through the majority of absorption troughs in Figure 1 would lie well above the $L\alpha$, N V, Si IV, and C IV absorption troughs, which suggests a lower contribution in these regions (e.g., due to absorption features in the unocculted spectrum). On the other hand, this continuum would lie well below the level required to account for our measured low covering factor for the Mg II absorption. In addition, at the densities required for the presence of the Fe II metastable absorption ($> 10^6$ cm $^{-3}$; Wampler, Chugai, & Pettijean 1995) or the C III metastable absorption ($> 10^9$ cm $^{-3}$; Bromage et al. 1985), the Si II fine-structure line at 1533.4 Å (Figure 1b) should be twice as strong as the Si II resonance line at 1526.7 Å (Flannery, Rybicki, & Sarazin 1980), and it does not appear to be so. The only simple solution to this dilemma is that both of these lines are saturated and the flux of unocculted light is greater underneath the fine-structure line (i.e, a broad C IV emission feature in the unocculted spectrum).

Thus, the unocculted spectrum must consist of continuum, broad emission lines, and broad absorption lines similar to those of the nuclear spectrum itself. The most straightforward explanation is that there is a scattering region that is outside of the region responsible for the D+E component, which reflects a fraction of the nuclear spectrum into our line of sight. This is a reasonable conclusion, given evidence for electron-scattered radiation in many Seyfert 2 galaxies (Moran et al. 2000, and references therein) and the troughs of broad absorption-line (BAL) QSOs (Ogle et al. 1999). Additional evidence for electron scattering of the nuclear radiation in NGC 4151 comes from ground-based spectropolarimetry, which finds significant ($\sim 1\%$) polarization in the continuum and broad emission lines in relatively large ($\sim 3''$) apertures (Schmidt & Miller 1980; Axon et al. 1994; Martel 1998). Henceforth, we will refer to the unocculted emission in our echelle spectra as “scattered light”.

Since electron scattering is independent of wavelength, the spectrum of the scattered light in NGC 4151 should be the nuclear spectrum averaged over some time interval (except

for possible velocity shifts or broadening due to thermal or bulk motion of the scatterers). However, the extreme variability of the UV spectrum of NGC 4151 (Ulrich et al. 1991) and the rather loose limits on the location of the scattering region imposed by our aperture size (projected distances $< 0''.1$ or 6.4 pc from the central continuum source) make it difficult to determine what the time-averaged spectrum should look like. Given that NGC 4151 was in moderate to high states for at least 7 years prior to the STIS echelle observations (Weymann et al. 1997; Paper I) and evidence that the low-ionization absorption lines appear at only low continuum flux levels (Paper I), the most reasonable assumption is that the scattered spectrum resembles NGC 4151 in (at least) a moderate flux state and, hence, contains only the high-ionization broad absorption lines.

We have adopted our STIS low-dispersion spectrum, which was obtained in 1998 at a high state and covers the entire UV region at high signal-to-noise (Nelson et al. 2000a; Paper I), as the basis of our scattered spectrum. In fitting the scattered light profile, different scale factors are needed for different continuum regions and emission lines. For the continuum, we find that the best scale factors increase linearly from 0.12 to 0.20 over the 1150 – 3100 Å region. We find scale factors of 0.12 for the high-ionization emission lines (e.g., C IV, N V, Si IV) and 0.4 for the low-ionization lines (e.g., Mg II, C III], the Fe II emission complex beginning at 2300 Å). Nevertheless, there is observational justification for different scale factors. The time-averaged nuclear spectrum is likely to reflect a lower state than our high-state spectrum, and the variability amplitudes of the low-ionization emission lines are much smaller than those of the continuum or high-ionization emission lines (Clavel et al. 1990). Also, the variability amplitude of the continuum in NGC 4151 (and other Seyfert 1 galaxies) decreases with wavelength in the UV (Crenshaw et al. 1996). Thus, larger scale factors are appropriate for the low-ionization emission lines and the long-wavelength continuum regions.

We show our scattered-light spectrum beneath the STIS echelle spectra in Figure 3 (a – c, the upper fit to the continuum and broad emission will be discussed later). Qualitatively, the scattered-light spectrum provides a good match to the troughs of the broad absorption lines. In particular, the scattered spectrum no longer falls above the troughs of the high-ionization absorption lines, and it matches the troughs of absorption lines embedded in various emission lines reasonably well. For example, although the Mg II absorption appears not to be saturated at first glance, the scattered-light spectrum shows that the $\lambda 2796.3$ line is indeed saturated. Furthermore, tests show that inclusion of narrow Mg II emission in the nuclear spectrum, which should be present at the systemic redshift of NGC 4151 (Nelson et al. 2000a), would saturate the Mg II $\lambda 2803.5$ absorption as well. Although the scattered-light spectrum does not provide a perfect match to the troughs of the saturated lines, we conclude that there is a significant flux of scattered light ($\sim 12\%$ of the high-state FUV continuum) within the aperture, and that most of the broad absorption lines in the echelle

spectra must be highly saturated, indicating large ionic columns. In the observed low state, the percentage of light that is scattered is therefore very high (e.g. $\sim 50\%$ in the long wavelength continuum).

2.3. Absorption Measurements

In this paper, we focus on the narrow kinematic components A, C, and E', and on the broad component D+E, since these components are likely to be photoionized (directly or indirectly) by the central continuum source. In addition, we present results on a new component mentioned in Paper I, which we will call D'; this component is shallow, broad (FWHM ≈ 940 km s $^{-1}$), highly blueshifted (-1680 km s $^{-1}$), and only seen in the high ionization lines (N V, C IV, and Si IV). The D' component is not detected in previous STIS or GHRS spectra obtained at higher states but it is clearly seen as a flattening of the C IV absorption profile around 1544 Å in the STIS echelle spectra (Paper I). Figure 4 shows the D' component in the N V $\lambda 1238.8$ absorption. This component was isolated by matching the D+E component with the profile derived from S II $\lambda 1253.8$ (Figure 2) and then subtracting this fit (in optical depth space) from the broad observed blend.

We do not provide results on components B, F, and F' in this paper. Component B is from our Galaxy, and components F and F' are likely to arise from the interstellar medium and/or halo of NGC 4151 (Weymann et al. 1997); detailed analyses of these components will be provided in Danks et al. (2000).

To determine the shape of the intrinsic continuum, we used a simple spline fit to regions that appeared free of absorption or emission. Similarly, several broad emission-line profiles were fit with cubic splines in regions unaffected by absorption, and an “average” broad profile was adopted (clearly this is a simplification, since the broad emission lines do not necessarily have the same profile in individual sources). This profile was then reproduced at the known positions of each broad line, and scaled in flux until a suitable match was obtained. Our resulting estimate of the intrinsic continuum plus emission spectrum is given as the upper plot in Figure 3.

Measurements of the narrow absorption components A, C, and E' are straightforward, since the absorption lines are relatively unsaturated and resolved (i.e., FWHM > 10 km s $^{-1}$). Here we assume that these components cover the entire continuum plus broad emission regions. Since the residual intensities of the narrow components are large, a non-unity covering factor would have only a minor effect on the derived columns. Each absorption-line profile is converted to optical depth as a function of radial velocity, and integrated to obtain

the ionic column density (Crenshaw et al. 1999). Velocity centroids and widths (FWHM) are also determined from the optical depth profiles (see Table 1).

Measurements of the broad absorption lines are more complicated. It is extremely difficult to separate Weymann et al.’s D and E components (contrary to our expectations in Paper I), because they are broad and blended together. The velocity centroids of all the isolated broad lines are very similar, which indicates that both components are present in each line, and it is therefore not possible to isolate the D or E component in a particular line. Since any differences in the observed profiles of different ions can be explained by saturation effects, contamination by other lines (particularly Fe II), or the scattered light spectrum, we can find no evidence that these components are physically distinct. We will therefore assume that this is one component (D+E). We used a cubic spline to fit the D+E component in the S II $\lambda 1253.8$ line, as shown in Figure 2.

Another complication is our finding that most of the broad (D+E) lines are heavily saturated. Although we have a qualitative idea of what the scattered spectrum looks like, we do not know the scattered flux beneath these lines exactly, and therefore it is not possible to determine their ionic column densities. The only relatively isolated lines that are not clearly saturated are S II $\lambda 1253.8$, Ni II $\lambda 1317.2$, and some of the metastable Fe II lines. We determined the velocity centroid and FWHM of D+E from these lines, and the column densities by integration of their optical depths. To obtain absolute lower limits on the D+E components of other isolated but saturated lines, we used optical depth profiles obtained by assuming no scattered light (i.e, a covering factor of 1.0). For doublets that are blended (e.g., C IV), we used the S II $\lambda 1253.8$ optical depth profile to match the two lines assuming the proper ratio of oscillator strengths.

We have retrieved the GHRS spectra of Weymann et al. (1997) from the *HST* archives to determine the column densities and velocities of the absorption components in a consistent fashion. We have also measured the absorption in a high-resolution STIS slitless spectrum of the C IV region observed on 1997 May 25 (Paper I). We list our measurements of the velocity centroid and FWHM of each component in the echelle spectra in Table 1. These values are consistent with those of Weymann et al. (1997), except that his component C is much broader (FWHM $\approx 140 \text{ km s}^{-1}$) than ours. Our own measurements of the GHRS and STIS spectra show no evidence for changes in the velocities and widths of any component that are larger than those expected from measurement and wavelength calibration errors (typically $\pm 10 \text{ km s}^{-1}$). We present a comparison of the slitless (STIS1), echelle (STIS2), and GHRS (epochs 1–5) ionic column densities and lower limits in Table 2.

3. Modeling The Absorbers

Photoionization models for this study were generated using the code CLOUDY90 (Ferland et al. 1998). We have modeled the absorbers as matter-bounded slabs of atomic gas, irradiated by the ionizing continuum radiation emitted by the central source. As per convention, the models are parameterized in terms of the ionization parameter, U , the ratio of the density of photons with energies ≥ 13.6 eV to the number density of hydrogen atoms (n_H) at the illuminated face of the slab. Each separate kinematic component was modeled with its own set of initial conditions, i.e., U , n_H , and the physical depth of the slab. As in earlier studies (e.g. Kriss 1998; Crenshaw & Kraemer 1999), a model is deemed successful when the predicted ionic column densities provide a good match (i.e., better than a factor of 2) to those observed.

The SED for the ionizing radiation in NGC 4151 is difficult to determine, due to the combined effects of intrinsic absorption in the UV (Kriss et al. 1992, 1995) and X-ray (George et al. 1998, and references therein). Although the narrow emission line ratios are sensitive to the SED, Alexander et al. (1999) and Kraemer et al. (2000a) demonstrated that there is evidence for considerable absorption between the central source and the NLR. Hence, while both Alexander et al. and Kraemer et al. argued against the presence of a “Big Blue Bump” at energies > 13.6 eV, the narrow lines cannot be used to constrain the SED. As a result, we have assumed the simple “intrinsic” SED described in Kraemer et al. (2000a), specifically a series of power-laws of the form $F_\nu \propto \nu^{-\alpha}$, with $\alpha = 1$ below 13.6 eV, $\alpha = 1.4$ over the range $13.6 \text{ eV} \leq h\nu < 1000 \text{ eV}$, and $\alpha = 0.5$ above 1000 eV.

As discussed in Paper I (and references therein), the UV continuum of NGC 4151 is highly variable. During the time of these observations, the extinction-corrected continuum flux at 1450 \AA was $f_{1450} = 1.1 \times 10^{-13} \text{ ergs cm}^{-2} \text{ s}^{-1} \text{ \AA}^{-1}$, assuming an extinction $E_{B-V} = 0.04$ (Kriss et al. 1995). This is roughly 25% of the flux of NGC 4151 in a “high” state, e.g. during the GHRs epoch 5 observations (Weymann et al. 1997). In several cases, we have compared our models of the current (“low” state) absorbers with the high state absorbers observed with the GHRs; in order to do so, we increased the ionizing flux by a factor of 4, while, for simplicity, using the same SED, although there is some evidence for variations in the latter as a function of continuum flux (Edelson et al. 1996).

Since $L\alpha$ is saturated for most of the kinematic components, the ionization state and effective hydrogen column density ($N_{eff} = N(\text{H I}) + N(\text{H II})$) of the absorbers is derived from the ionic columns of the heavy elements¹⁰ and, therefore, is sensitive to the elemental

¹⁰We use $N(\text{XM})$ to denote ionic columns, where “X” is the atomic symbol and “M” is the ionization

abundances. Since there is no strong evidence for unusual abundances in the nucleus of NGC 4151 (although see Kraemer et al. 2000a), we have assumed roughly solar element abundances (cf. Grevesse & Anders 1989). They are, by number relative to H, as follows: He = 0.1, C = 3.4×10^{-4} , N = 1.2×10^{-4} , O = 6.8×10^{-4} , Ne = 1.1×10^{-4} , Mg = 3.3×10^{-5} , Al = 2.96×10^{-6} , Si = 3.1×10^{-5} , P = 3.73×10^{-7} , S = 1.5×10^{-5} , Fe = 4.0×10^{-5} , and Ni = 1.78×10^{-6} . We have assumed that the gas is free of cosmic dust, hence all the elements are fully in the gas phase.

4. Comparison of the Observations and Model Results

4.1. Component A

GHRS spectra of Component A revealed absorption by C IV, Mg II, and Si II (Weymann et al. 1997). Kriss (1998) was able to match the Mg II and C IV columns with a single-component photoionization model, with $U = 0.001$ and $N_{eff} = 2.0 \times 10^{18} \text{ cm}^{-2}$. The STIS2 data show absorption from the following ions: H I, Si II, Si III, Si IV, C II, C IV, and Mg II. We detected both C II $\lambda 1334$ and C II* $\lambda 1336$; the ratio of $N(\text{C II})/N(\text{C II}^*)$ is ≈ 1.2 , indicating that n_e (electron density) is $\sim 100 \text{ cm}^{-2}$ (Srianand & Petitjean 1999), which is consistent with the $N(\text{Si II})/N(\text{Si II}^*)$ ratio, within the errors. After Shields & Hamann (1997), the C IV recombination timescale is $t \sim (n_e N(\text{C IV})/N(\text{C III}) \alpha_{C IV})^{-1}$. Using $\alpha_{C IV}$ (the radiative recombination rate) from Shull & van Steenberg (1982), t is ~ 800 yrs. We measured a C IV column of $(4.1 \pm 0.3) \times 10^{13} \text{ cm}^{-2}$, which is close to the earlier GHRS results (see Table 2) as expected, given the long recombination time. The Mg II and Si II columns are identical to those from GHRS epoch 5, within the measurement errors.

We were able to fit the ionic columns densities of A in the STIS2 spectra with a single component photoionization mode assuming $U = 0.0012$, and $N_{eff} = 1.3 \times 10^{18} \text{ cm}^{-2}$, similar to Kriss (1998). The model predictions are compared to the measured columns in Table 3 (note that the model predicts total ionic columns, rather than separate predictions for ground and excited states of ions). The predictions matched the measured columns quite well, although $N(\text{Si III})$ is overpredicted, which may be due to the difficulty in determining the profile of the blue wing of $L\alpha$.

As shown in Table 2, between GHRS epochs 4 and 5 there was a significant drop in the Mg II and Si II columns. Given the low densities derived for Component A, these changes are most likely the result of transverse motion, rather than a response to changes in the

state.

ionizing continuum. We were able to match the GHRs epoch 4 results by adding a second component, with $U = 0.0003$ and $N_{eff} = 4 \times 10^{17} \text{ cm}^{-2}$; assuming the two components are at the same radial distance, the additional component would have a density of $\sim 400 \text{ cm}^{-3}$. The additional low ionization gas contributes no C IV absorption, as required by the lack of variation of $N(\text{C IV})$. This component must have a transverse velocity of $\sim 2000 \text{ km s}^{-1}$ in order to pass out of our line of sight to the broad line region (BLR) within 1.5 years, assuming the BLR of NGC 4151 is 4 light days in diameter (Clavel et al. 1990); this is not unreasonable, considering that the radial velocity of Component A is $\sim 1588 \text{ km s}^{-1}$.

4.2. Component C

Both C IV and Mg II absorption lines were identified with Component C in the GHRs spectra (Weymann et al. 1997). Based on these ionic columns, Kriss (1998) modeled the absorber as a single slab with $U = 0.002$ and $N_{eff} = 1.25 \times 10^{18} \text{ cm}^{-2}$. Our re-examination of the GHRs spectra revealed the presence of absorption by Si II $\lambda 1526$ in Epoch 1. In addition to these ions, the STIS2 spectra show absorption from Si III, Si IV, and C II. Based on the upper limit for C II* $\lambda 1336$, $N(\text{C II}^*)/N(\text{C II})$ is ~ 0.2 , which indicates $n_e \sim 10 \text{ cm}^{-2}$. At such low densities, Si II* $\lambda 1533$ should be weak or absent (Flannery et al. 1980), which is indeed the case. Also, the ionic columns should not respond to the changes in ionizing flux, which is true for Mg II, Si II, and C IV (Table 2).

We modeled Component C as a single slab, with $U = 0.0012$, and $N_{eff} = 1.0 \times 10^{18} \text{ cm}^{-2}$. The model predictions and measured ionic columns for are listed in Table 4. Most of the ionic columns are well fit, albeit with overpredictions of Si III (see above) and Si II.

4.3. Component D+E

As noted in Section 2, we have not tried to deconvolve the Weymann et al.’s Components D and E. The cumulative absorption component (D+E) possesses strong high ionization lines, e.g. N V, C IV, and Si IV. In our STIS2 spectra, a number of lower ionization absorption lines are associated with Component D+E, the most striking of which are those from metastable levels of Fe II (Paper I), including those with lower levels up to 4.1 eV above the ground state. With the resolution of the STIS echelle, we have now established that the C III* $\lambda 1175$ absorption, which arises from a level 6.5 eV above the ground state, is also associated with D+E, indicating densities of $n_e \geq 10^9 \text{ cm}^{-3}$.

The population of metastable states of C III and Fe II likely result from collisional

excitation (although, for a discussion of the excitation of Fe II metastable states by UV radiation, see Verner et al. [1999]). The relative populations of the C III metastable, $^3P^o$, and ground, 1S_L states, as a function of n_e and temperature, have been calculated by Bromage et al. (1985) and Kriss et al. (1992). For a gas characterized by $n_e = 10^{9.5} \text{ cm}^{-3}$ and $T = 2 \times 10^4 \text{ K}$, a few percent of the C III will be in the excited state (while collision rates for temperatures below $2 \times 10^4 \text{ K}$ are unavailable at the time of this writing, it is probable that the relative population of the $^3P^o$ state will be smaller at lower temperatures). Under such conditions, *at least* the lowest 25 energy levels for Fe II ($\leq 2.64 \text{ eV}$ above the ground state) will be in statistical equilibrium (Verner et al. 1999). The ratio of Si II*/Si II cannot be used as a density indicator, since it is clear that these lines are saturated (see Section 2).

As discussed in Section 2, the measurement of the ionic column densities for Component D+E is hampered by the complex profile of the underlying scattered component and the fact that the lines from the most abundant ions are saturated. The only isolated unsaturated lines are S II $\lambda 1254$ (which has a weak oscillator strength, $f = 0.01$; Morton et al. 1988), Ni II $\lambda 1317$ (which has a low abundance; Section 3), and some of the weaker Fe II metastable lines. We have, therefore, used the S II and Ni II columns to constrain the fraction of low ionization gas in the absorber. Although there are no weak high ionization lines in the STIS data, P V $\lambda\lambda 1117.98, 1128.01$ has been detected in HUT Astro-1 and Astro-2 observations (Kriss et al. 1992; Kriss et al. 1995) and with the Berkeley spectrometer aboard *Orbiting and Retrievable Far and Extreme Ultraviolet Spectrometers (ORFEUS) - Shuttle Pallet Satellite (SPAS) II* mission (Espey et al. 1998). Based on the equivalent widths determined by Espey et al., and the appearance that the lines are unsaturated, $N(\text{P V})$ is $\approx 1.2 \times 10^{14} \text{ cm}^{-2}$. Since the ionization potentials of P IV and C III are similar (51.4 eV and 47.9 eV, respectively; Allen 1973), it is reasonable to expect that the ratio of ionic columns of P V and C IV will be approximately the same as that of the elemental abundances of phosphorus and carbon (i.e. 0.001; cf. Grevesse & Anders 1989). Hence, at the time of *ORFEUS-SPAS II* observations, during which NGC 4151 was in a high flux state, $N(\text{C IV})$ must have been $\sim 10^{17} \text{ cm}^{-2}$. Although there are no far-UV observations contemporaneous with the STIS echelle observations, we will show that it is plausible that the columns of C IV and P V have remained relatively constant since the time of the *ORFEUS-SPAS II* mission.

Based on these assumptions, we have modeled the Component D+E as a single slab, with $U = 0.015$, $n_H = 3.2 \times 10^9 \text{ cm}^{-2}$, and $N_{eff} = 2.75 \times 10^{21} \text{ cm}^{-3}$. The predicted and measured ionic columns are listed in Table 5. We ran two models, one assuming thermal broadening and the other a microturbulence velocity of 435 km s^{-1} , and found no significant differences in the predicted ionic column densities (the results we discuss are from the former model). The model is successful in reproducing the Ni II and S II columns, within the measurement errors. In all other cases, with the exception of Al III, the model predictions exceed the

lower limits for the ionic column densities, which is a *necessary, but insufficient test* of the model. The predicted average electron temperature is $\sim 1.6 \times 10^4 \text{K}$, hence our assumption that fractional population of the $^3\text{P}^o$ state of C III is $\sim 1\%$ is reasonable. The predicted $N(\text{Al III})$ is close to the derived upper limit, which may indicate that the Al III lines are not highly saturated, or that the aluminum may exceed solar, as has been suggested for BALQSOs (Shields 1997).

As an additional test of the model, we ran a high state version, increasing U by a factor of 4 (see above), while holding N_{eff} fixed. The results are listed in Table 5, alongside the low state model predictions. Notably, the Fe II and Si II columns are small enough that their absorption lines would be weak or below the limit of detectability, which is precisely the case for the STIS1 (Paper I) and GHRIS (Weymann et al. 1997) observations, which were all obtained at a high state. On the other hand, Mg II absorption would still be present; the predicted column density is similar to that seen in GHRIS epoch 5 (which we determined to be $\approx 1.0 \times 10^{14} \text{cm}^{-2}$). The higher ionization lines, such as N V $\lambda\lambda 1238, 1241$ and C IV $\lambda\lambda 1548, 1551$, would remain heavily saturated, and hence do not change appreciably in profile, as is the case (see Paper I). Most important, the C IV column density does not change significantly, while N(P V) is close to the value derived from the *ORFEUS - SPAS II* observations. Therefore, given this model solution, it is possible to use the high state value of N(P V) to constrain N_{eff} . Although there may be other possible solutions, we will show in section 4.4 that the physical conditions in Component D' depend strongly on the column density and ionization state of Component D+E, and hence provide a further test.

4.4. Component D'

The appearance of Component D' was discussed in Section 2.3, and, as noted, it is present in N V, C IV, and Si IV (see Table 6). Since $N(\text{Si IV}) = 4.5 \times 10^{14} \text{cm}^{-2}$, there must be a significant column of C III, although no corresponding C III* $\lambda 1175$ is detected, indicating that the electron density is $< 10^{9.5} \text{cm}^{-3}$. Assuming that this component is directly ionized, we were unable to fit the measured ionic columns with a single-component model. Our best fit was a two component model, with the C IV and Si IV absorption arising in one component ($U = 0.001$; $N_{eff} = 2 \times 10^{20} \text{cm}^{-2}$), and the N V arising in more highly ionized gas ($U \geq 0.1$, $N_{eff} \geq 1 \times 10^{20} \text{cm}^{-2}$). However, if the ionizing flux is increased by a factor of 4, the C IV column predicted by the lower ionization component *increases*, due to the ionization of the large C III column; hence a directly ionized, multi-component model does not predict the absence of Component D' while NGC 4151 is in a high state.

The coincidence of the appearance of D' at the same time as the low ionization lines

from D+E can be best explained if the former is screened by the latter. To demonstrate this, we generated a single-component model, with $N_{eff} = 1 \times 10^{20} \text{ cm}^{-2}$, using the ionizing continuum filtered by D+E as the input spectrum (see Figure 5a). In order to reproduce the observed high ionization lines, assuming that these components are at the same approximate radial distance, the D' component must have $U = 0.012$, which yields a density of $n_H = 2.6 \times 10^7 \text{ cm}^{-3}$. As shown in Table 6, the model predictions provide a good fit to the N V, C IV, and Si IV columns, and indicate that Si II and Mg II lines should be weak or absent (due to the small column densities and broadness of this feature). A second model was generated, using the filtered continuum from the high state model for Component D+E as the input (Figure 5b), while holding n_H and N_{eff} fixed, which results in $U = 4.15$. The results are listed in the 3rd column of Table 6 and, as required by the observations, the predicted column densities are quite small. Therefore, the appearance of D' while NGC 4151 was in its low state is the direct result of the higher EUV opacity of D+E .

4.5. Component E'

Component E', isolated kinematically by Weymann et al. (1997), is a low ionization absorber, as evidenced by the presence of Mg II $\lambda 2803$ and absence of C IV $\lambda\lambda 1548, 1551$. Based on these constraints Kriss (1998) determined the ionization parameter for this component to be $U < 0.0004$, with $N_{eff} \sim 10^{17} - 10^{18} \text{ cm}^{-2}$. In addition to Mg II, we have found absorption lines of O I, C II, Si II, and Fe II associated with this component, but, as with the GHRS results, no high ionization lines (Table 7). Interestingly, all of the ionic species present arise from states with ionization potentials below 13.6 eV. Among the more interesting features is the presence of absorption by the fine structure line O I* $\lambda 1304$ (in addition to the ground state line O I $\lambda 1302$). The ratio of $N(\text{O I}^*)/N(\text{O I})$ is ≈ 0.64 , which is close to the ratio of the statistical weights of the two levels, indicating that they are in collisional equilibrium. Based on the transition probabilities and collision strengths (Pradhan & Peng 1995, and references therein), Component E' must have $n_e \geq 10^6 \text{ cm}^{-3}$. This is consistent with the density indicated by the $N(\text{Si II}^*)/N(\text{Si II})$ ratio, ~ 2 , within the measurement errors, requiring $n_e > 10^3$ (Flannery et al. 1980).

We modeled E' as a single slab, with $U = 0.0001$, $n_H = 1 \times 10^6 \text{ cm}^{-3}$, and $N_{eff} = 1.5 \times 10^{18} \text{ cm}^{-2}$. The model predictions are listed in Table 7, and show good agreement with the measured ionic columns. The predicted Fe II column is greater than that measured, which is evidence for a substantial population in metastable states, as one would expect at this density (Wampler et al. 1995) (the metastable Fe II lines were not detected in our spectra, due to their substantially lower oscillator strengths). A high state comparison model was

run, with U increased by a factor of 4. The predictions for $N(\text{Mg II})$ and $N(\text{Si II})$ were $6.7 \times 10^{12} \text{ cm}^{-2}$ and $1.3 \times 10^{13} \text{ cm}^{-2}$, respectively, in good agreement with the GHRIS epoch 4 values (see Table 2). This indicates the increase in ionic column density of the low ionization lines between GHRIS4 and STIS2 is likely due to a decrease in the ionizing flux. The columns for the high ionization lines remain small, e.g., $N(\text{C IV}) = 7.4 \times 10^{12} \text{ cm}^{-2}$, which would make them difficult to detect.

5. Discussion

5.1. The Geometry of the Circumnuclear Gas

The presence of absorption from both ground and fine structure absorption lines of O I, Si II, and C II in several kinematic component, and the absorption from metastable C III and Fe II in Component D+E, allows us to constrain the densities of the absorbers. Combined with the evidence for screening of Component D' by Component D+E, and a significant contribution from an unocculted scattering region, we can begin to define the structure of the circumnuclear gas in NGC 4151.

Based on the flux near the Lyman limit and our assumed SED, the number of ionizing photons emitted by the central source is $Q = 2 \times 10^{53} \text{ s}^{-1}$. From our determination of their densities¹¹ and ionization parameters, we place the absorbers at the following radial distances: Component C, 2.15 kpc; Component A, 681 pc; Component E', 23.6 pc, and Component D+E, 0.03 pc. As noted in the previous sections, we have assumed that Components A, C, and E' are directly ionized by the central source, and hence not screened by intervening gas. However, it is entirely plausible that A and C are screened by Component D+E. To test this, we generated models for these components using the high state filtered continuum (Figure 5), and found little change in the resulting column densities. The main effect is that these components would lie at $\sim 2/3$ the radial distance determined from the direct ionization models. Due to its greater density, Component E' must respond to short timescale flux and opacity changes, and we were unable to model the small observed changes in the ionic columns by assuming that this component is screened by D+E. Therefore, we suggest that E' is directly ionized, but not in our line-of-sight to the BLR and central source and, instead, is only occulting scattering emission¹² (which contributes $1/3 - 1/2$ of the UV

¹¹Note that the densities for Components D+E and E' are lower limits.

¹²If this is the case then the changes in the measured ionic columns over the last several years could at least partially be a result of an increased contribution of the scattered continuum to the total UV flux.

flux in the STIS2 data; see Section 2.2). Based on our model results, the absorbers decrease in density with increasing radial distance, faster than distance⁻² up to Component A. The relative positions of the absorbers and the scattering region are shown in Figure 6.

5.2. The Scatterer

Based on our analysis of the scattered profile, we can begin to constrain the physical characteristics of the scatterer. Assuming isotropic scattering by free electrons (see Section 2.2), for small electron scattering optical depths ($\tau < 1$), the reflected fraction of continuum radiation is $\approx N_e F_c \sigma_{thompson}$ (the product of the column density of free electrons, the covering factor, and the Thompson cross-section, respectively). In order to scatter $\sim 15\%$ of the UV radiation (see Section 2), the scatterer must have $N_e \sim 2 \times 10^{23} \text{ cm}^{-2}$ (for a covering factor of unity). From STIS G430M spectra taken on May 15, 2000, we determined that the total broad + narrow $H\beta$ flux from the central $0''.1$ was $\approx 5.8 \times 10^{-12} \text{ ergs s}^{-1} \text{ cm}^{-2}$ (Nelson et al. 2000b), or $L_{H\beta} \approx 1.2 \times 10^{41} \text{ ergs s}^{-1}$ (the distance to NGC 4151 is 13.3 Mpc, assuming $H_o = 75 \text{ km s}^{-1} \text{ Mpc}^{-1}$). Since reverberation mapping indicates that the broad-line emission arises in relatively dense gas (cf. Clavel et al. 1990), which will not contribute large columns of free electrons, we may assume that the scatterer makes only a small contribution (i.e., $< 10\%$) to the broad $H\beta$ emission. Since the total $H\beta$ emission depends on the number of recombinations per unit volume, this provides an upper limit to the density. Assuming Component D+E is $\approx 0.03 \text{ pc}$ from the nucleus, and does not cover the scattering region, we may assume that the scatterer is coincident or lies further from the nucleus, e.g., 0.1 pc . Finally, this component cannot be opaque to the ionizing radiation, since there is strong evidence that the NLR is powered by the central source (Alexander et al. 1999; Nelson et al. 2000a; Kraemer et al. 2000a). With these constraints, the scatterer can be characterized with the following parameters¹³: $U \geq 4.5$, $N_{eff} = 2 \times 10^{23} \text{ cm}^{-2}$, and $n_H \leq 1.0 \times 10^6 \text{ cm}^{-3}$. Recent *Chandra* High Energy Transmission Grating spectra of NGC 4151 reveal an extended ($\sim 1.6 \text{ Kpc}$), X-ray emission line region (Ogle et al. 2000), comprised of a two-phased medium: a hot (10^7K), collisionally ionized plasma, in which high ionization lines such as Fe XXV 1.79 \AA arise, and photoionized gas at temperatures $\leq 4 \times 10^4\text{K}$, which give rise to emission lines and radiative recombination continua from lower ionization species. It is possible that scatterer is part of the hot medium, although Ogle et al. find little scattered continuum below 3 keV.

¹³The temperature at the illuminated face of this component is $2.2 \times 10^5\text{K}$, hence it is not thermally stable (Krolik, McKee, & Tarter 1981)

5.3. The X-ray absorber

The scatterer model predicts large O VII, O VIII, Ne IX, and Ne X columns ($9.7 \times 10^{19} \text{ cm}^{-2}$, $2.3 \times 10^{19} \text{ cm}^{-2}$, $1.7 \times 10^{19} \text{ cm}^{-2}$, and $3.5 \times 10^{18} \text{ cm}^{-2}$, respectively), and, hence would appear as a “warm absorber” if viewed in our line-of-sight. This leads to the question whether the X-ray absorber and the scatterer are the same component, as suggested by Krolik & Kriss (1995) for Seyfert galaxies in general. This is particularly interesting since none of the UV components possesses sufficient X-ray opacity to account for the observed X-ray absorption. For example, Component D+E has the greatest column density and highest ionization parameter, but it transmits a considerable fraction of the intrinsic continuum at energies $> 300 \text{ eV}$ (see Figures 5a and 5b), which is clearly not observed in NGC 4151 (George et al. 1998). Furthermore, as noted above, the scatterer must have a high covering factor, and hence, it is likely that it covers the central source. To address this, we examined the *ASCA* observations of NGC 4151 from 1993 November 5. Since NGC 4151 was in a higher flux state at this time than during the STIS2 observations, we can assume that the scatterer was in at least as high a state of ionization as the one we have modeled. However, the predicted ratios of $N(\text{O VIII})/N(\text{O VII})$ and $N(\text{Ne X})/N(\text{Ne IX})$ are too large to fit the absorption profile in the *ASCA* data, and the fit cannot be improved by varying the fraction of scattered light, column density of the scatterer, or the X-ray photon index (Γ). Instead, the best fit parameters are as follows: $U = 0.86$, $N_{eff} = 4 \times 10^{22} \text{ cm}^{-2}$, $\Gamma = 1.5$, and a scattered fraction of ≈ 0.045 of the intrinsic flux (for the details of the analysis and fitting statistics, see George et al. 1998). The predicted ionic column densities for the X-ray absorber are listed in Table 8. The model predicts large C IV and N V columns, and hence could explain some of the UV absorption. Nevertheless, $N(\text{P V})$ and $N(\text{Mg II})$ are too low, even for a high state period, hence we believe that this component is not responsible for the bulk of the UV absorption. Furthermore, the C IV and N V absorption from the X-ray absorber could be buried in the deep D+E absorption trough, and hence undetectable, as suggested by Kriss et al. (1992). In summary, in addition to the UV absorbers and highly ionized scatterer, there is a third component of gas along our line-of-sight with an intermediate ionization parameter that produces the bulk of the X-ray absorption, similar to the multi-phased NLR suggested by Ogle et al. (2000).

The decoupling of the X-ray and UV absorption presents a problem: if the absorbers occult the same continuum source, they must screen one another. We ran a series of photoionization models to test the effects of screening. If the X-ray absorber is screened by the Component D+E, we found it will drop significantly in ionization as the continuum flux drops and the screening gas becomes increasingly opaque to the ionizing radiation, similar to the case for Component D'. However, we find no evidence of the huge low ionization columns (e.g. $N(\text{Ni II}) \geq 10^{16} \text{ cm}^{-2}$) which would arise from the X-ray absorber in such

a situation. Hence, in this scenario, the X-ray absorber must be of such low density that it does not respond on timescales of several years (i.e., $n_H < 10^3 \text{ cm}^{-3}$) which, in turn, requires that the short timescale variations in the X-ray absorption (Weaver et al. 1994; George et al. 1998) are due solely to transverse motion. On the other hand, if the X-ray absorber screens Component D+E from the ionizing source, as the ionizing flux dropped, we found that the UV absorber becomes far too neutral, unless the columns density of the X-ray absorber decreases by at least a factor of 4.

Although we cannot rule out the possibility that the UV and X-ray absorbers screen one another, we suggest another scenario. If the regions producing the UV and X-ray continua are not equally extended, each region could be covered by the respective absorber, i.e., the UV absorber covers the UV source and the BLR clouds, while the X-ray absorber covers only the X-ray source. Since the UV absorber must cover the BLR (~ 4 light days; Clavel et al. 1990), the simplest picture would have the X-ray absorber closer to the central source, occulting a smaller X-ray emitting region. The problem with this scenario is that the fraction of scattered light is apparently smaller in the X-ray than in the UV (~ 0.04 versus ~ 0.15 at a high state). However, this could be the result of 1) a (relatively) anisotropic X-ray continuum, as compared to the UV or 2) an isotropic X-ray absorber inside the radius of the scattering region, which modifies the X-ray continuum before it reaches the scattering region. In the latter case, a larger scattered light contribution would be necessary to fit the *ASCA* data. Since our fit to the UV data requires the presence of absorption profiles in the scattered light, and there is evidence for the presence of an X-ray absorber inside the NLR of NGC 4151 (Kraemer et al. 2000a), it would not be surprising that the scattered X-ray continuum would show strong absorption features.

6. Summary

We have used medium resolution echelle spectra obtained with *HST*/STIS to study the physical conditions in the intrinsic UV absorbers in the Seyfert 1 galaxy, NGC 4151, while it was in a recent low continuum state. The present paper is a detailed study following our observational results from Paper I. We have determined the following regarding the circumnuclear gas in NGC 4151.

1. Each of the kinematic components can be modeled as a single slab of atomic gas, of roughly solar elemental abundances, ionized by the EUV – X-ray continuum radiation emitted by the central source. The combined kinematic component D+E, which we have not attempted to deconvolve, has the largest column density ($2.75 \times 10^{21} \text{ cm}^{-2}$) and ionization parameter ($U = 0.015$) of the absorbers. The C III and Fe II metastable lines arise in this

component, indicating it is also the densest ($n_H \geq 3 \times 10^9 \text{ cm}^{-3}$) and closest to the ionizing source. Component D' , which was not detected in earlier high state spectra, appears to be screened from the nuclear source by Component D+E; it becomes too highly ionized to detect as the opacity of D+E decreases when NGC 4151 enters a high flux state. Our model predictions match the observed changes in the ionic columns; specifically that the denser components D+E, D' , and E' responded to the decrease in continuum flux since the time of the GHRS spectra, while the low density components A and C, have not (as a result of their long recombination timescales). None of the UV absorbers has sufficient X-ray opacity to produce the observed X-ray absorption.

2. We have been able to constrain the densities of the UV absorbers based on the ratios of fine structure to ground state C II, O I, and Si II lines, and the presence of lines from metastable states of C III and Fe II. From these densities, and the ionization parameters determined from the fits to the ionic column densities, we can determine the relative radial positions of the individual absorbers, as shown in Figure 6. Based on these results, it is apparent that the UV absorbers extend over a large range in radial distances, and decrease in density with distance.

Weymann et al. (1997) found that the radial velocities of Components A and C had changed little between GHRS epochs 2 and 5. From this, they determined the limit for steady radial acceleration for Component A to be $\sim 1 \times 10^{-3} \text{ cm s}^{-2}$. Assuming that the cloud is optically thin, and a mean observed continuum flux for NGC 4151, this limit requires that Component A lies at a radial distance of $\geq 0.7 \text{ pc}$. Since the distances we have determined for Components A, C, and E' are all significantly greater than this limit, we find no apparent conflicts with the Weymann et al.'s conclusions. Since Component D+E lies much closer to the nuclear source, one might expect that it should experience a noticeable acceleration. However, since D+E is optically thick in the Lyman continuum and has a large column density, it is probable that radiative acceleration will be less efficient (Williams 1972; Mathews 1974). Additionally, the evidence for transverse motion in the UV and X-ray is evidence for more complex dynamics, which we intend to address in a subsequent paper.

3. Based on the residual flux in the troughs of saturated absorption lines associated with Component D+E, we estimate that at least 15% of the high-state continuum emission, broad emission lines, and absorption lines are scattered into our line of sight, from a plasma that extends outside the solid angle subtended by the absorber (in Figure 6 we show a possible location for the scatterer). For a covering factor of unity, the scatterer must have a free electron column density of $N_{eff} \sim 2 \times 10^{23} \text{ cm}^{-2}$. Based on the constraints on the total $H\beta$ flux, the covering factor, and the EUV opacity of the scatterer, we argue that it must be highly ionized ($U \geq 4.5$) and, hence, cannot produce the observed X-ray

absorption. Instead, a smaller column of lower ionization gas ($N_{eff} = 4 \times 10^{22} \text{ cm}^{-2}$, $U = 0.86$) must also be present. There are several possibilities regarding the relative position of this additional component with respect to the UV absorbers and scatterer. Also, the reason for the apparent differences in the fractions of UV and X-ray scattered light remains an open question, which can be better addressed through simultaneous UV (*HST*/STIS) and X-ray (*Chandra*) observations of NGC 4151.

S.B.K. and D.M.C. acknowledge support from NASA grant NAG5-4103. We thank Fred Bruhweiler, Tahir Yaqoob, and Jane Turner for enlightening discussions.

REFERENCES

- Alexander, T., Sturm, E., Lutz, D., Sternberg, A., Netzer, H., & Genzel, R. 1999, *ApJ*, 512, 204
- Allen, C.W. 1973, *Astrophysical Quantities* (London: Athlone)
- Antonucci, R.R.J., 1993, *ARA&A*, 31, 473
- Axon, D.J., Hough, J.H., Young, S., & Inglis, M. 1994, *Ap&SS*, 216, 379
- Barr, P., White, N.E., Sanford, P.W., & Ives, J.C. 1977, *MNRAS*, 181, 43P
- Barvainis, R. 1987, *ApJ*, 320, 537
- Boksenberg, A., Snijders, M.A.J., Wilson, R., Benvenuti, P., Clavel, J., Macchetto, F., Penston, M., Boggess, A., Gull, T.R., & Gondhalekar, P. 1978, *Nature*, 275, 404
- Bromage, G.E., et al. 1985, *MNRAS*, 215, 1
- Clavel, J., Boksenberg, A., Bromage, G.E., Elvius, A., Penston, M.V., Perola, G.C., Santos-LLeo, M., Snijders, M.A.J., & Ulrich, M.-H. 1990, *MNRAS*, 246, 668
- Clavel, J. et al. 1987, *ApJ*, 321, 251
- Crenshaw, D.M., & Kraemer, S.B. 1999, *ApJ*, 521, 572
- Crenshaw, D.M., Kraemer, S.B., Boggess, A., Maran, S.P., Mushotzky, R.F., & Wu, C.-C. 1999, *ApJ*, 516, 750
- Crenshaw, D.M., Kraemer, S.B., Hutchings, J.B., Danks, A.C., Gull, T.R., Kaiser, M.E., Nelson, C.H., & Weistrop, D. 2000b, *ApJ*, in press (Paper I)
- Crenshaw, D.M., Kraemer, S.B., Hutchings, J.B., Bradley, L.D. II, Gull, T.R., Kaiser, M.E., Nelson, C.H., Ruiz, J.R., & Weistrop, D. 2000a, *ApJ*, in press
- Crenshaw, D.M., et al. 1996, *ApJ*, 470, 322
- Danks, A.C., et al. 2000, in preparation
- deVaucouleurs, G., et al. 1991, *Third Reference Catalog of Bright Galaxies* (New York: Springer).
- Edelson, R.A., et al. 1996, *ApJ*, 470, 364
- Evans, I.N., Tsevatnov, Z., Kriss, G.A., Ford, H.C., Caganoff, S., & Koratkar, A.P. 1993, *ApJ*, 417, 82
- Espey, B.R., Kriss, G.A., Krolik, J.H., Zheng, W., Tsvetanov, Z., & Davidsen, A. 1998, *ApJ*, 500, L13
- Ferland, G.J., et al. 1998, *PASP*, 110, 761

- Flannery, B.P., Rybicki, G.B., & Sarazin, C.L. 1980, *ApJS*, 44, 539
- George, I.M., Turner, T.J., Netzer, H., Nandra, K., Mushotzky, R.F., & Yaqoob, T. 1998, *ApJS*, 114, 73
- Grevesse, N., & Anders, E. 1989, in *Cosmic Abundances of Matter*, ed. C.J. Waddington (New York: AIP), 1
- Hamann, F., Barlow, T.A., Junkkarinen, V., & Burbidge, E.M. 1997, *ApJ*, 478, 80
- Holt, S.S., Mushotzky, R.F., Becker, R.H., Boldt, E.A., Serlemitsos, P.J., Szymkowiak, A.E., & White, N. E. 1998, *ApJ*, 241, L13
- Kraemer, S.B., & Crenshaw, D.M. 2000, *ApJ*, 532, 256
- Kraemer, S.B., Crenshaw, D.M., Hutchings, J.B., Gull, T.R., Kaiser, M.E., Nelson, C.H., & Weistrop, D. 2000, *ApJ*, 531, 278.
- Kraemer, S.B. et al., 2000b in preparation
- Kriss, G.A. 1998, in *The Scientific Impact of the Goddard High Resolution spectrograph*, ed. J.C. Brandt, T.B. Ake, & C.C. Petersen (San Francisco: Astronomical Society of the Pacific), ASP Conference Series, 143, 271
- Kriss, G.A., Davidsen, A.F., Zheng, W., Kruk, J.W., & Espey, B.R. 1995, *ApJ*, 454, L7
- Kriss, G.A., et al. 1992, *ApJ*, 392, 485
- Krolik, J.H., & Kriss, G.A. 1995, *ApJ*, 447, 512
- Krolik, J.H., McKee, C.F., & Tarter, B. C. 1981, *ApJ*, 249, 422
- Martel, A. 1998, *ApJ*, 508, 657
- Mathews, W.G. 1974, *ApJ*, 189, 23
- Moran, E.C., Barth, A.J., Kay, L.E., & Filippenko, A.V. 2000, *ApJ*, 540, L73
- Morton, D.C., York, D.G., & Jenkins, E.B. 1988, *ApJS*, 68, 449
- Nelson, C.H., Weistrop, D., Hutchings, J.B., Crenshaw, D.M., Gull, T.R., Kaiser, M.E., Kraemer, S.B., & Lindler, D. 2000a, *ApJ*, 531, 257
- Nelson, C.H. et al. 2000b, in preparation
- Ogle, P.M., Cohen, M.H., Miller, J.S., Tran, H.D., Goodrich, R.W., & Martel, A. 1999, *ApJS*, 125, 1
- Ogle, P.M., Marshall, H.L., Lee, J.C., & Canizares, C.R. 2000, *ApJ*, in press
- Perola, G.C., et al. 1982, *MNRAS*, 200, 293
- Perola, G.C., et al. 1982, *ApJ*, 306, 508

- Pradhan, A.K., & Peng, J. 1994, in *Atomic Data for the Analysis of Emission Lines: A Meeting in Honor of the 70th Birthdays of D.E. Osterbrock and M.J. Seaton*, Proceedings of the STScI Symposium Held in Baltimore, MD. May 16 - 18, 1994; ed. R. Williams & M. Livio (Cambridge University Press), 8
- Reynolds, C.S. 1997, *MNRAS*, 286, 513
- Schmidt, G.D, & Miller, J.S. 1980, *ApJ*, 240, 759
- Shields, G.A., 1997, in *Mass Ejection from AGN*, ed. N. Arav, I. Shlosman, & R.J. Weymann (San Francisco: Astronomical Society of the Pacific), ASP Conference Series, 128, 214
- Shields, J.C., & Hamann, F. 1997, *ApJ*, 481, 752
- Shull, J.M, & van Steenberg, M. 1982, *ApJS*, 48, 95
- Silvis, J., & Bruhweiler, F.C. 2000, in preparation
- Srianand, R., & Petitjean, P. 2000, *A&A*, 357, 414
- Ulrich, M.-H., Altamore, A., Perola, G.C., Boksenberg, A., Penston, M.V., Snijders, M.A.J., Bromage, G.E., Clavel, J., & Elvius, A. 1985, *Nature*, 313, 747
- Ulrich, M.-H., Boksenberg, A., Penston, M.V., Bromage, G.E., Clavel, J., Elvius, A., Perola, G.C., & Snijders, M.A.J. 1991, *ApJ*, 382, 483
- Verner, E.M, Verner, D.A., Korista, K.T., Ferguson, J.W., Hamann, F., & Ferland, G.J. 1999, *ApJS*, 120, 101
- Wampler, E., Chugai, N.N., Petitjean, P. 1995, *ApJ*, 443, 586
- Weaver, K.A., Yaqoob, T., Holt, S.S., Mushotzky, R.F., Matsuoka, M., & Yamauchi, M. 1994, *ApJ*, 436, L27
- Weymann, R.J., Morris, S.L., Gray, M.E., & Hutchings, J.B. 1997, *ApJ*, 483, 717
- Williams, R.E. 1972, *ApJ*, 178, 105
- Yaqoob, T., Warwick, R.S., & Pounds, K.A. 1989, *MNRAS*, 236, 153

Fig. 1.— STIS echelle spectra of the nucleus of NGC 4151; the spectra have been smoothed by a boxcar function of 7 pixels for display purposes. Identifications of the broad absorption lines associated with D+E, except for Fe II, are given above the spectra. Fe II multiplets are plotted below the spectra, with the length of each vertical line representing the gf value from Silvas & Bruhweiler (2000).

Fig. 2.— Plots of the Si IV $\lambda 1393.8$ and S II $\lambda 1253.8$ lines as functions of radial velocity (with respect to the nucleus of NGC 4151 at a redshift of 0.00332). The spectra have been normalized by dividing by the continuum plus emission fit (Figure 3). The expected positions of the absorption components are plotted as vertical dotted lines. The smooth line in the lower plot is our fit to the D+E component of S II; note there may be a slight contamination at -100 to $+300$ km s $^{-1}$ due to an Fe II line from multiplet UV CW. Component B is Galactic, and Components F and F' are most likely from the interstellar medium or halo of NGC 4151.

Fig. 3.— STIS echelle spectra of NGC 4151. The lower plots give our estimate of the scattered light spectrum (see text). The upper plots give our continuum plus broad-emission fits to the echelle spectra.

Fig. 4.— Plot of the N V $\lambda 1238.8$ absorption as a function of radial velocity. The upper smooth plot gives our fit to the D' component, the lower smooth plot gives the sum of the D' and D+E components. The location of N V emission from the narrow-line region (NLR) is noted. The scattered component has not been subtracted in this plot.

Fig. 5.— The incident (solid line) and transmitted (dotted line) continua for the models of Component D+E: a) the low flux state model and b) the high flux state model (see text, Section 4.4). The flux values for the incident continuum are in $\log(\nu F_\nu)$ at the face of the slab (in units of ergs s $^{-1}$ cm $^{-2}$).

Fig. 6.— Schematic diagram of the nuclear region of NGC 4151, showing the relative positions of the central source, the emission-line bicone, and the UV absorbers. The viewing angle relative to the bicone is given by the kinematic model by Crenshaw et al. (2000a). The dotted line represents a possible radial position and distribution of the scattering medium, although the only real constraint is that it is not completely covered by D+E in projection.

Table 1. Absorption Components in NGC 4151

Component	Centroid (km s ⁻¹)	FWHM (km s ⁻¹)
A	-1588 (±8)	36 (±4)
B	-1025 (±5)	— ^a
C	-858 (±8)	27 (±3)
D+E	-491 (±8)	435 (±12)
D'	-1680 (±85)	940 (±60)
E'	-215 (±11)	59 (±8)
F	-16 (±4)	34 (±4)
F'	+34 (±4)	15 (±1)

^asensitive to saturation level, see Danks et al. (2000).

Table 2. Comparison of Component Ionic Columns ($\times 10^{13} \text{ cm}^{-2}$) from STIS and GHRSSpectra^a

	GHRSS1 22.06.92 ^b	GHRSS2 04.07.92	GHRSS3 03.01.94	GHRSS4 28.10.94	GHRSS5 11.03.96	STIS1 25.05.97	STIS2 15.07.99
Line	Comp. A						
Si II $\lambda 1526$	1.22 (± 0.22)					<0.20	0.46 ^c (± 0.08)
Si II* $\lambda 1533$	1.17 (± 0.22)	0.97 (± 0.24)	1.05 (± 0.19)	1.27 (± 0.28)	0.51 (± 0.16)	<0.20	0.53 ^d (± 0.08)
C IV $\lambda 1548$		2.83 (± 0.31)	3.62 (± 0.34)	3.90 (± 0.17)	3.84 (± 0.22)	3.13 (± 0.18)	4.11 (± 0.31)
Mg II $\lambda 2796$			0.46 (± 0.03)	0.48 (± 0.04)	0.29 (± 0.03)		0.27 (± 0.04)
Line	Comp. C						
Si II $\lambda 1526$	0.29 (± 0.13)					0.32 (± 0.12)	0.46 ^c (± 0.06)
Si II* $\lambda 1533$	<0.20	<0.20	<0.20	<0.20	<0.20	<0.20	<0.20
C IV $\lambda 1548$		2.21 (± 0.37)	2.65 (± 0.32)	2.79 (± 0.41)	2.67 (± 0.25)	2.50 (± 0.43)	2.95 (± 0.40)
Mg II $\lambda 2796$			0.09 (± 0.03)	0.11 (± 0.02)	0.12 (± 0.03)		0.10 (± 0.03)
Line	Comp. E'						
Si II $\lambda 1526$	<0.20	<0.20	<0.20	0.34 (± 0.11)	<0.20	<0.20	1.37 (± 0.19)
Si II* $\lambda 1533$	<0.20	<0.20	<0.20	0.63 (± 0.17)	<0.20	<0.20	2.45 (± 0.31)
C IV $\lambda 1548$	<0.30	<0.30	<0.30	<0.30	<0.30	<0.30	<0.30
Mg II $\lambda 2803$			0.61 (± 0.09)	0.68 (± 0.06)	0.64 (± 0.06)		1.90 (± 0.13)

^ablank entry: not in wavelength coverage. Values in parentheses are the measurement errors for the previous line

^bObservation date (UT) in Day.Month.Year.

^cfrom Si II $\lambda 1260.4$.

^dfrom Si II* $\lambda 1264.7$.

Table 3. Predicted and Observed Ionic Columns ($\times 10^{13} \text{ cm}^{-2}$) for Component A

Ion (Line)	Model ^a Prediction	Measured Column
H I (L- α)	8.12E+02	$> 1.0\text{E}+01^b$
C II ($\lambda 1334$)		3.43 (± 0.53)
C II* ($\lambda 1336$)		4.19 (± 0.46)
C II (total)	7.42	7.62 (± 0.70)
C III	3.25E+01	
C IV ($\lambda 1548$)	3.84	4.11 (± 0.31)
Mg II ($\lambda 2796$)	0.21	0.27 (± 0.03)
Mg II ($\lambda 2803$)	0.21	0.29 (± 0.05)
Si II ($\lambda 1260$)		0.46 (± 0.08)
Si II* ($\lambda 1265$)		0.53 (± 0.15)
Si II (total)	0.93	0.99 (± 0.17)
Si III ($\lambda 1206$)	2.09	0.55 (± 0.07)
Si IV ($\lambda 1393$)	0.80	0.98 (± 0.12)
Si IV ($\lambda 1403$)	0.80	1.12 (± 0.22)
Fe II	0.02	

^aU = 0.0012, $N_{eff} = 1.3\text{E}+18 \text{ cm}^{-2}$.

^bSaturated.

Table 4. Predicted and Observed Ionic Columns ($\times 10^{13} \text{ cm}^{-2}$) for Component C

Ion (Line)	Model ^a Prediction	Measured Column
H I (L- α)	6.40E+03	
C II (λ 1334)	5.84	4.71 (\pm 0.36)
C III	2.50E+01	
C IV (λ 1548)	2.88	2.95 (\pm 0.40)
C IV (λ 1551)	2.88	3.20 (\pm 0.44)
Mg II (λ 2796)	0.17	0.07 (\pm 0.01)
Mg II (λ 2803)	0.17	0.10 (\pm 0.03)
Si II (λ 1260)	0.76	0.30 (\pm 0.06)
Si III (λ 1206)	1.57	0.58 (\pm 0.05)
Si IV (λ 1393)	0.61	0.51 (\pm 0.07)
Si IV (λ 1403)	0.61	0.70 (\pm 0.17)

^aU = 0.0012, $N_{eff} = 1.0\text{E}+18 \text{ cm}^{-2}$.

Table 5. Predicted and Observed Ionic Columns ($\times 10^{13} \text{ cm}^{-2}$) for Component D + E

Ion (Line ^a)	Model ^b Prediction	Highstate ^c Prediction	Measured Column
H I (L- α)	6.4E+06	1.6E+04	
C II	2.0E+04	1.43E+01	
C III* λ 1175	3.9E+02 ^d	5.0E+01	> 3.8E+01
C IV	2.5E+04	3.1E+04	> 4.3E+02
N V	1.5E+03	7.9E+03	> 2.7E+02
O I	2.9E+04	—	
Mg II	1.6E+03	6.3	> 3.4E+01
Al III	1.1E+02	3.4	> 1.2E+02
Si II (λ 1526)			> 1.3E+02
Si II* (λ 1533)			> 8.8E+01
Si II (total)	2.1E+03	0.21	> 2.2E+02
Si III (λ 1206)	1.7E+03	2.7E+01	> 1.6E+02
Si IV	1.9E+03	2.1E+02	> 1.1E+02
P V	7.7	6.5	1.2E+01 ^e
S II	6.3E+02	—	1.0E+03 (\pm 5.0E+02)
Fe II (λ 1608)	2.3E+03	—	> 1.7E+02 ^f
Ni II	1.1E+02	—	8.5E+01 (\pm 2.2E+01)

^awhen no wavelength is listed, the measured column is derived from a simultaneous fit to two or more lines (see text).

^b $U = 0.015$, $N_{eff} = 2.75\text{E}+21 \text{ cm}^{-2}$.

^c $U = 0.060$, $N_{eff} = 2.75\text{E}+21 \text{ cm}^{-2}$.

^dassuming $N_{metastable}/N_{ground} = 0.01$ (see text).

^evalue from *ORFEUS-SPAS II* observation (Espey et al. 1998).

^fdetermined from resonance lines.

Table 6. Predicted and Observed Ionic Columns ($\times 10^{13} \text{ cm}^{-2}$) for Component D'

Ion (Line ^a)	Model ^b Prediction	Highstate ^c Prediction	Measured Column
H I (L- α)	3.34E+04	3.33	
C II	8.54E+01	—	
C III	3.83E+02	—	
C IV	2.58E+02	0.19	1.20E+02 ($\pm 2.40\text{E}+01$)
N V	1.70E+02	0.97	2.20E+02 ($\pm 4.40\text{E}+01$)
Mg II	1.30	—	
Si II	3.26	—	
Si III	2.15E+01	—	
Si IV	2.82E+01	—	4.50E+01 (± 9.00)

^awhen no wavelength is listed, the measured column is derived from a simultaneous fit to two or more lines (see text).

^bscreened by Component D+E (see text), $U = 0.012$, $N_{eff} = 1.0\text{E}+20 \text{ cm}^{-2}$.

^cscreened by Highstate Component D+E (see text), $U = 4.15$, $N_{eff} = 1.0\text{E}+20 \text{ cm}^{-2}$.

Table 7. Predicted and Observed Ionic Columns ($\times 10^{13} \text{ cm}^{-2}$) for Component E'

Ion (Line)	Model Prediction ^a	Measured Column
H I (L- α)	8.83E+03	
C II (λ 1334)		9.73 (\pm 3.18)
C II* (λ 1335)		1.23E+01 (\pm 3.11)
C II (total)	3.56E+01	2.20E+01 (\pm 4.45)
C III	1.46E+01	
O I (λ 1302)		5.47 (\pm 2.54)
O I* (λ 1304)		3.48 (\pm 1.54)
O I (total)	6.26	8.95 (\pm 2.97)
Mg II (λ 2803)	2.03	1.90 (\pm 0.13)
Si II (λ 1526)		1.37 (\pm 0.19)
Si II* (λ 1533)		2.45 (\pm 0.31)
Si II (total)	3.75	3.82 (\pm 0.36)
Si III (λ 1206)	0.86	
Fe II (λ 2383)	2.31	0.50 (\pm 0.11)
Fe II (λ 2600)	2.31	0.31 (\pm 0.13)

^aU = 0.0001, $N_{eff} = 1.5\text{E}+18 \text{ cm}^{-2}$.

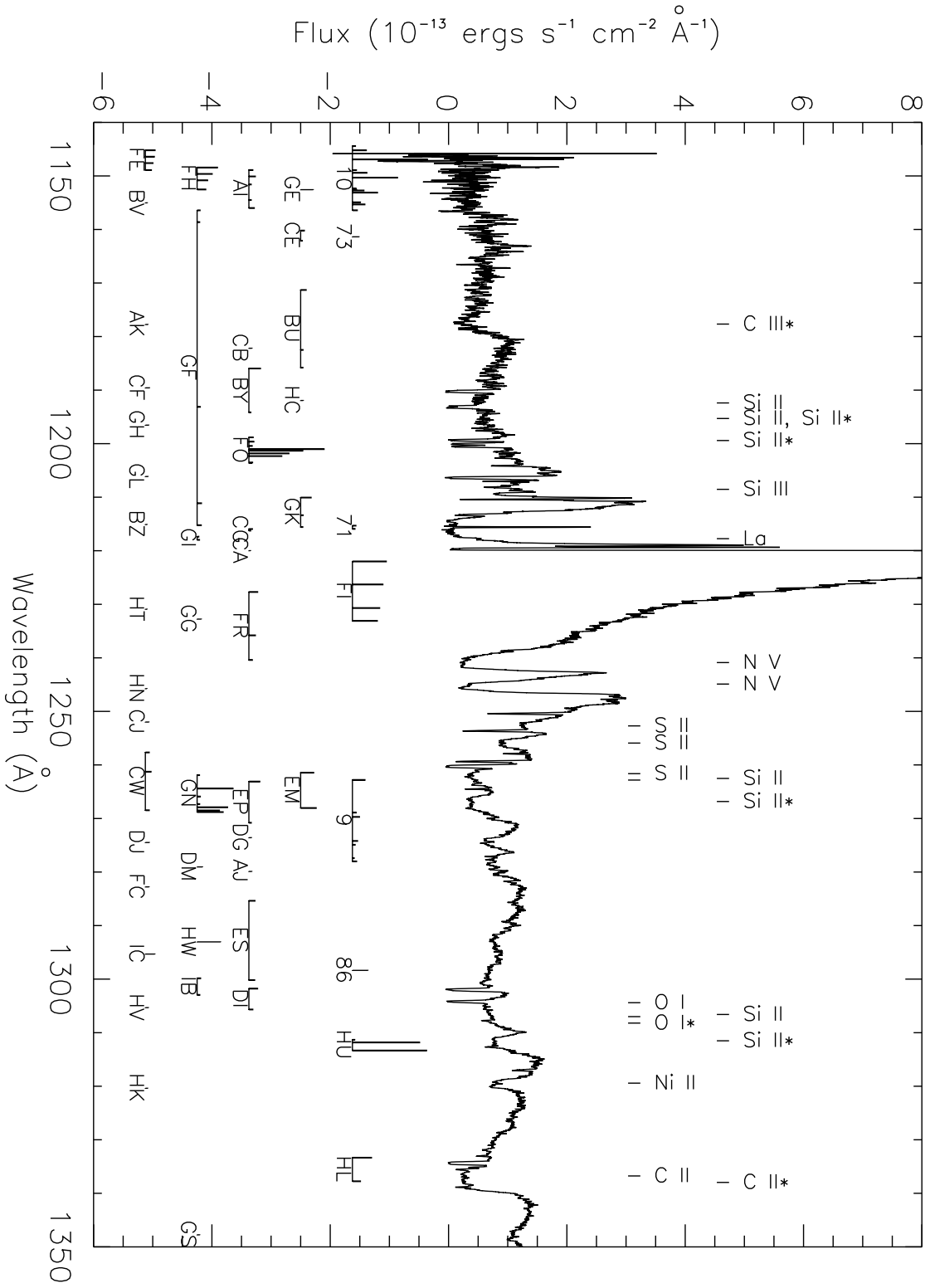


Fig. 1a.

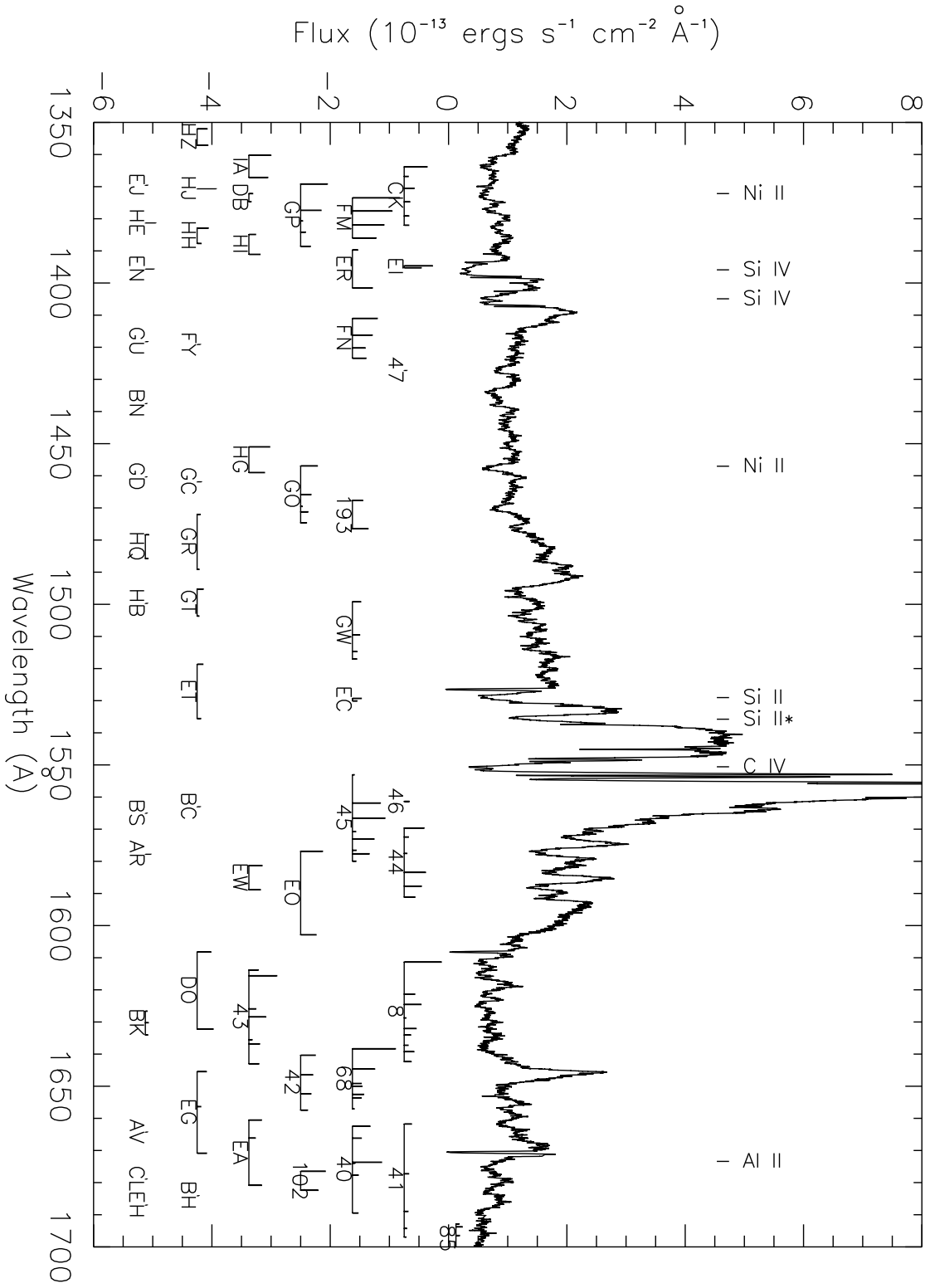


Fig. 1b.

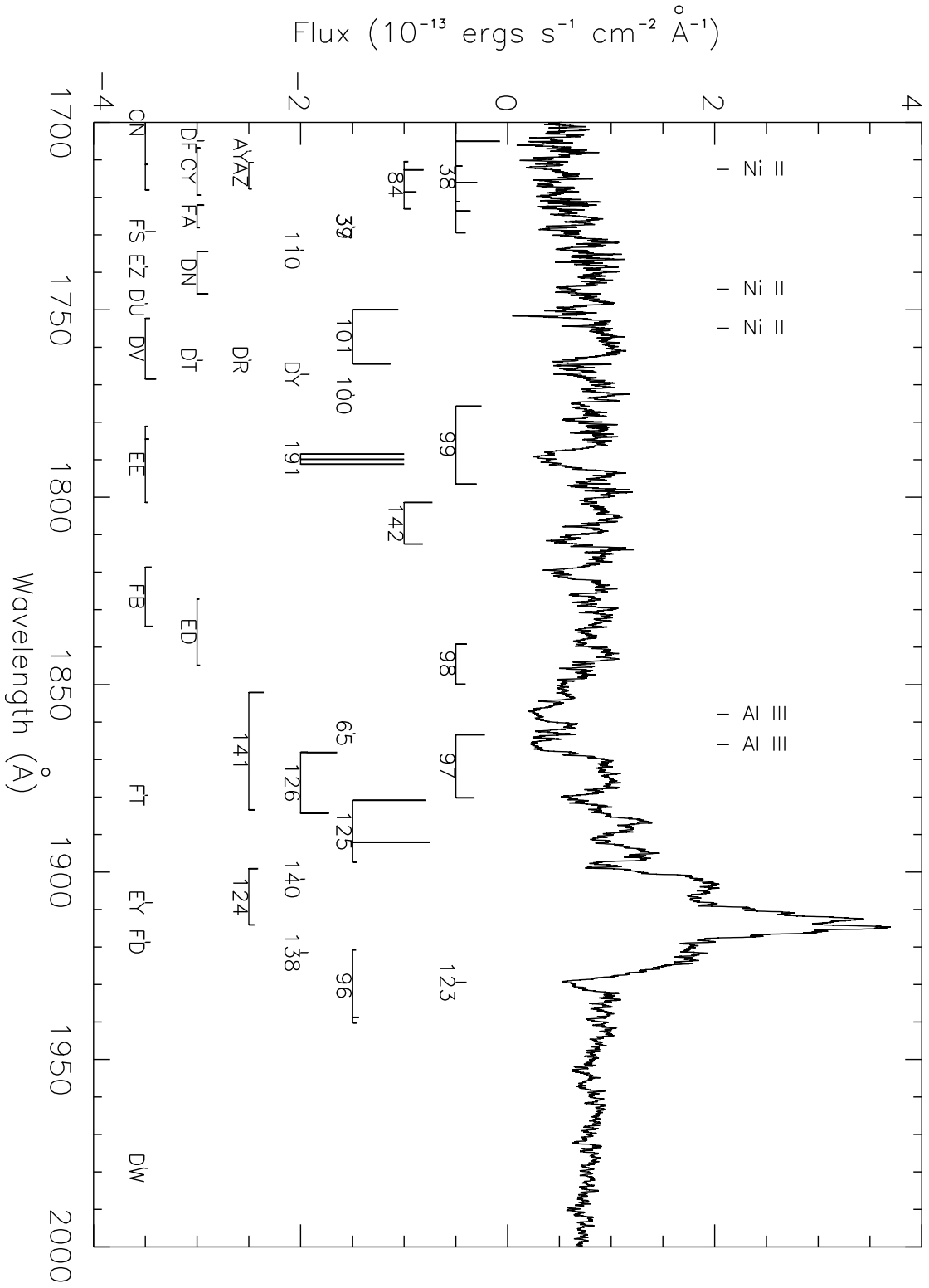


Fig. 1c.

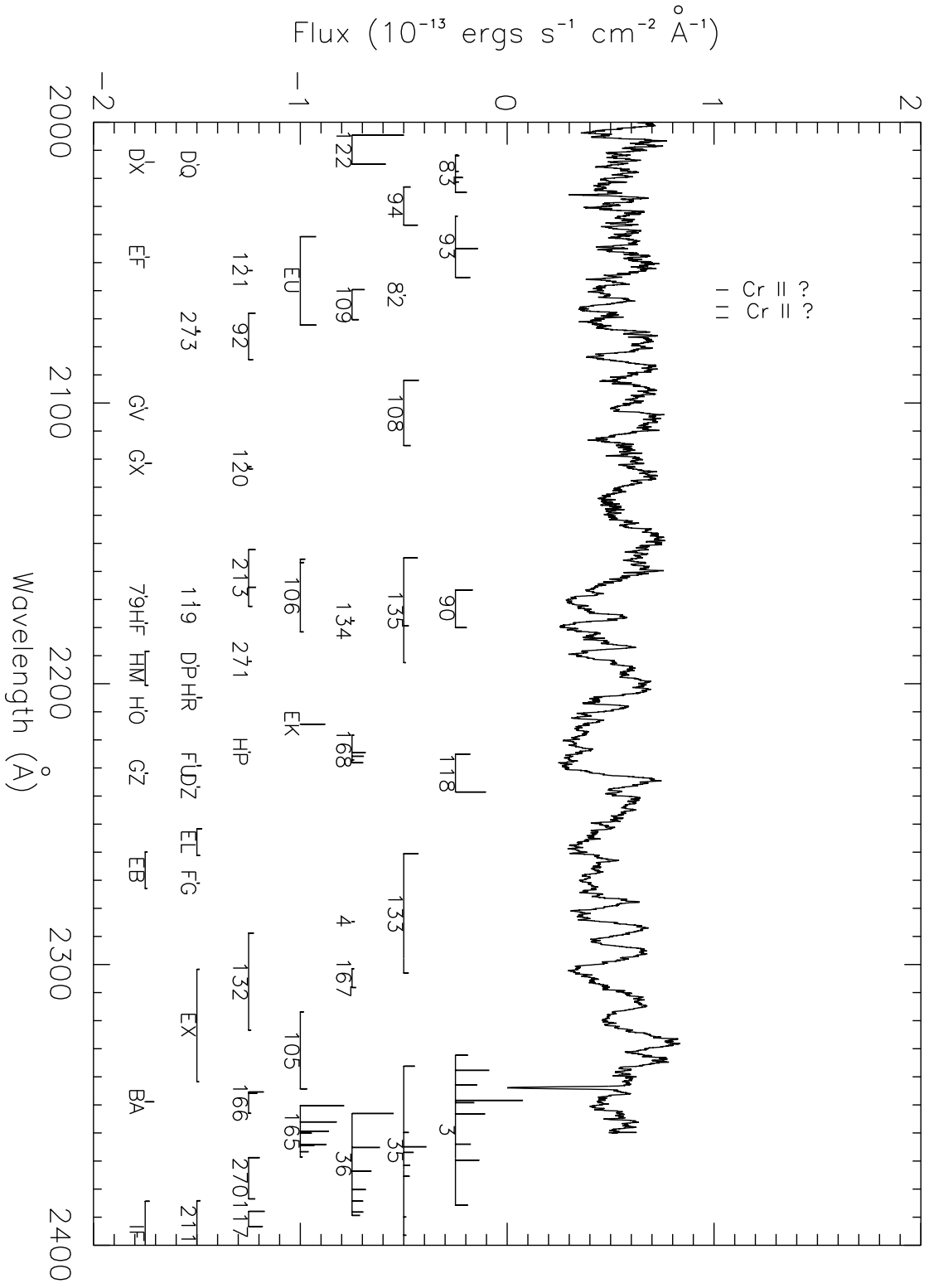


Fig. 1d.

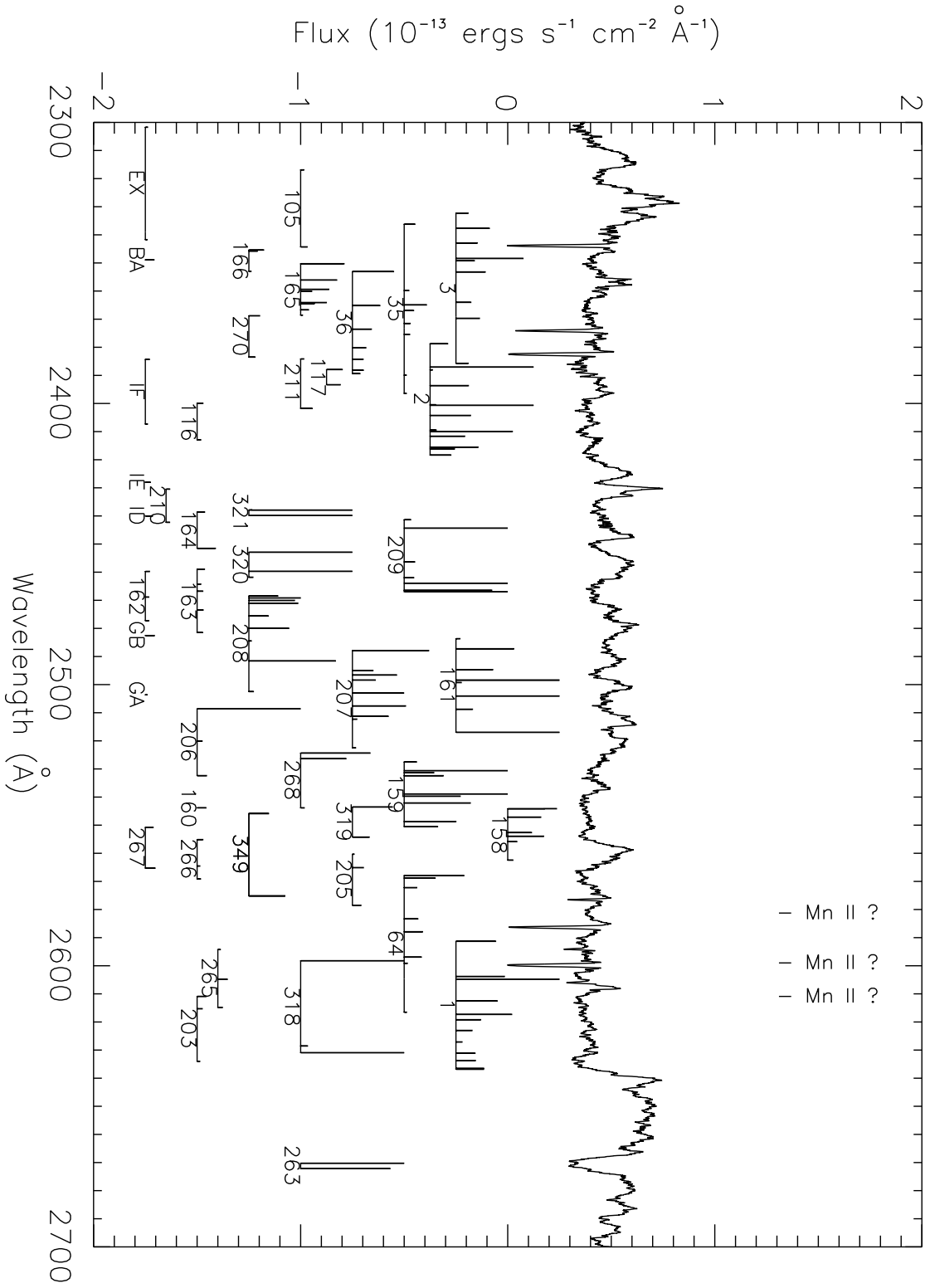


Fig. 1e.

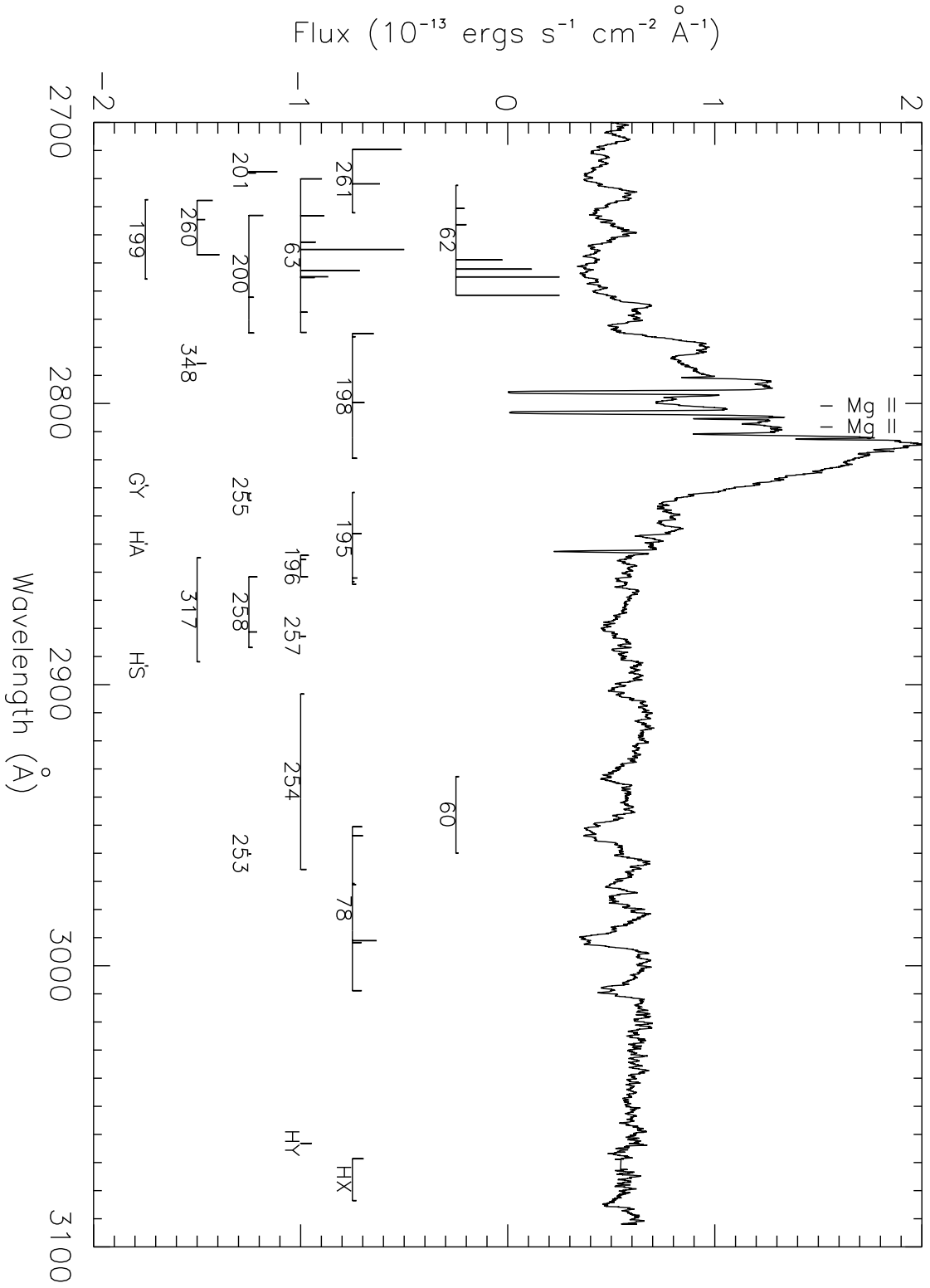


Fig. 1f.

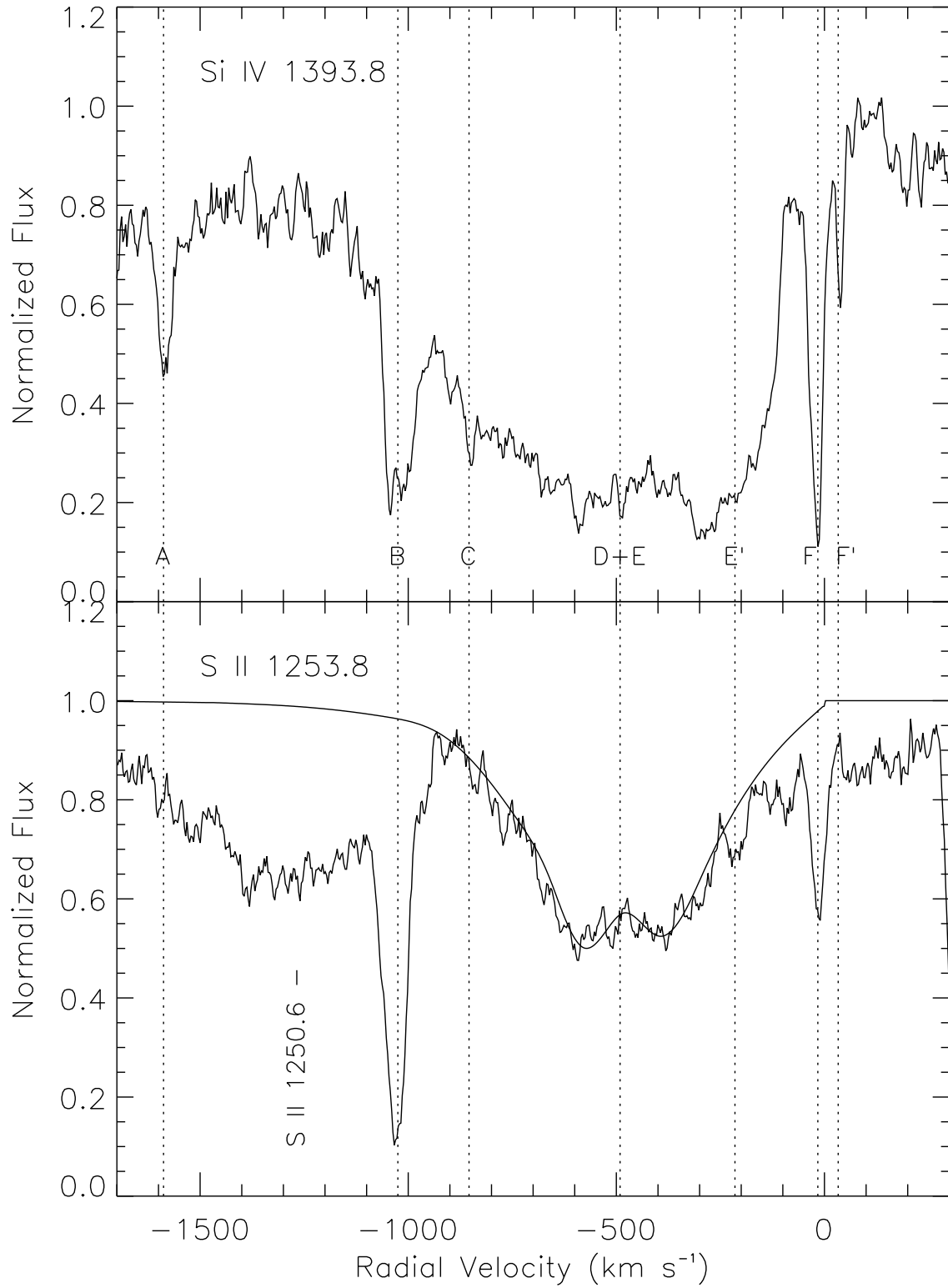


Fig. 2.

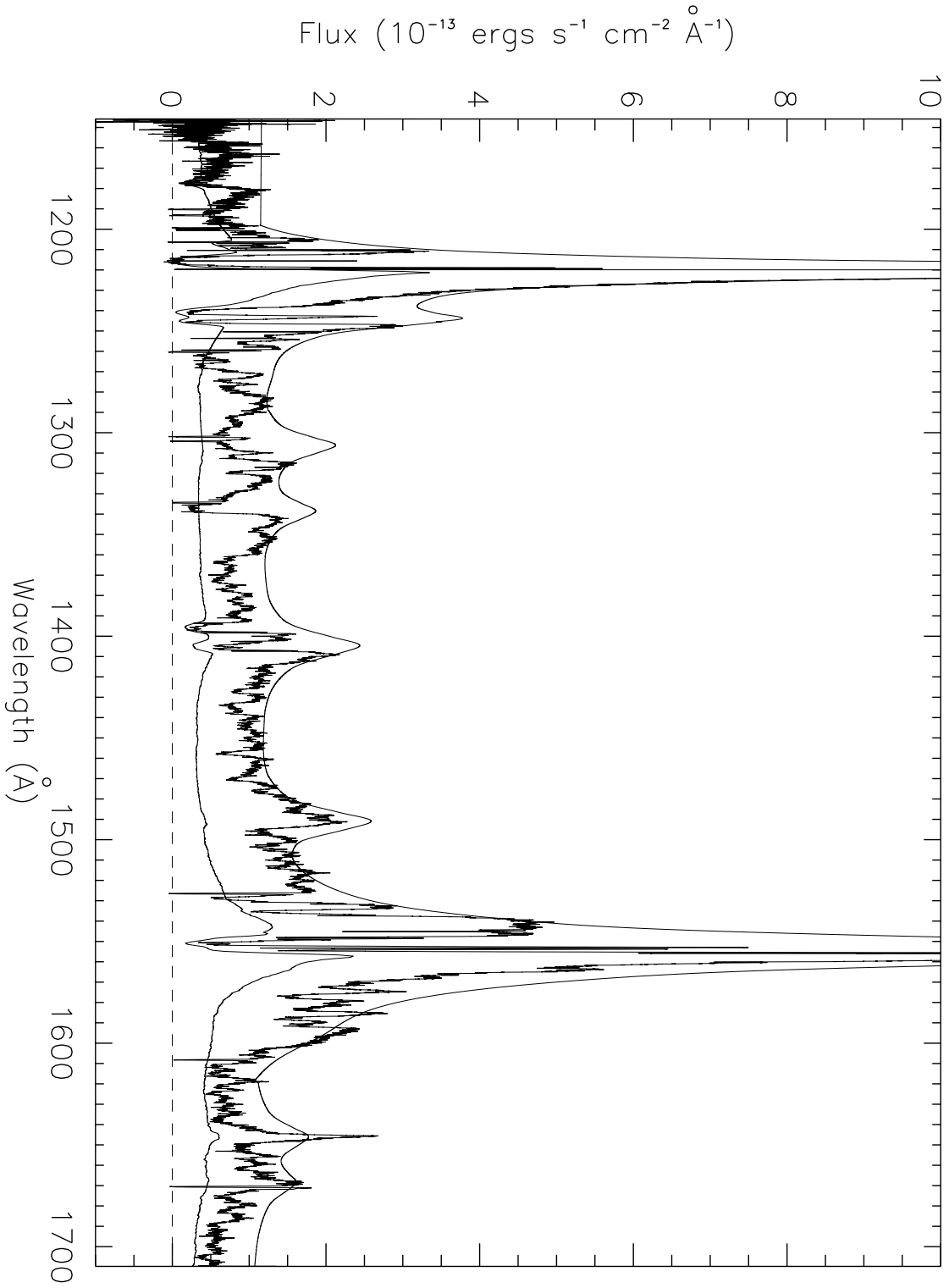


Fig. 3a.

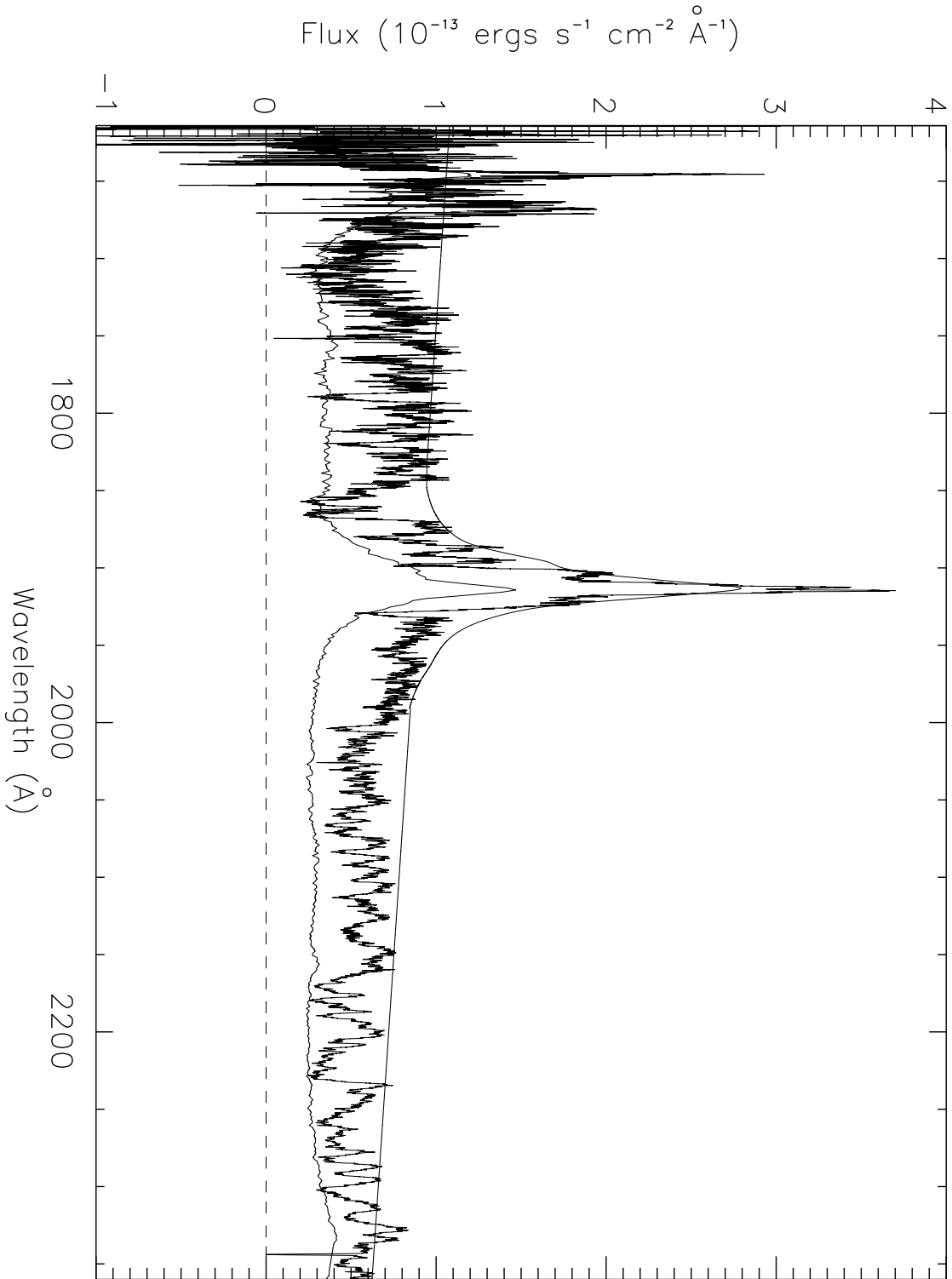


Fig. 3b.

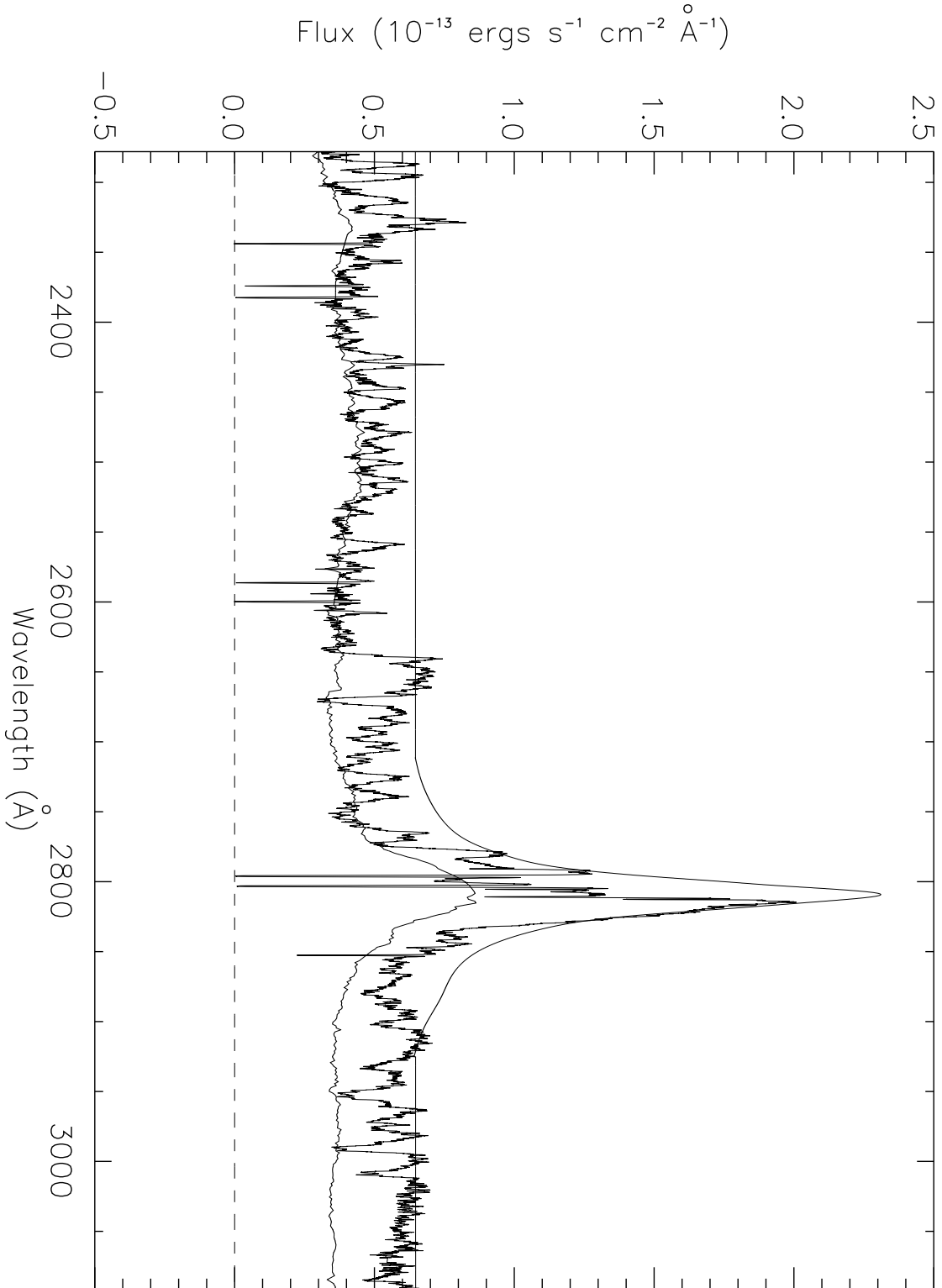


Fig. 3c.

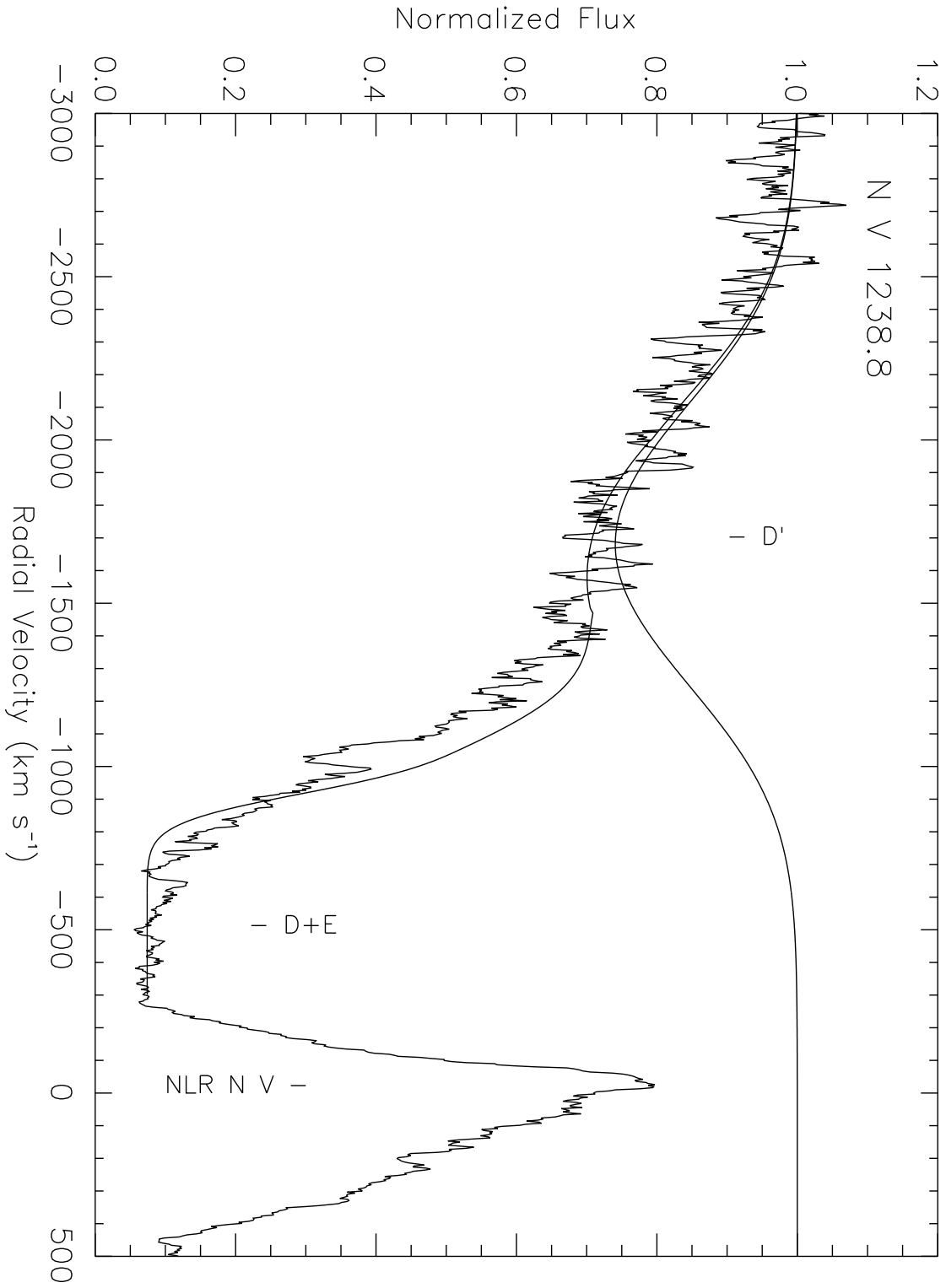


Fig. 4.

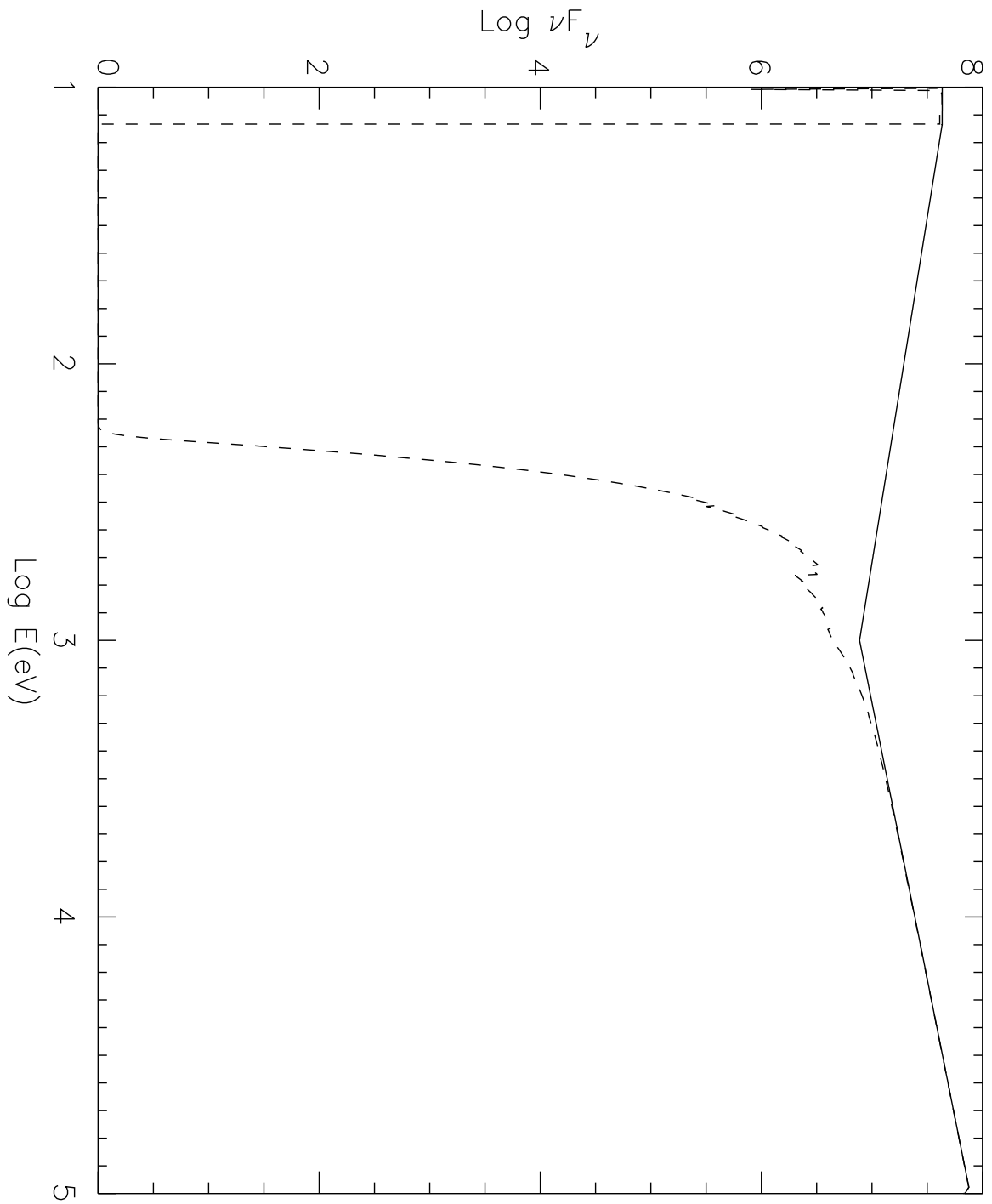


Fig. 5a.

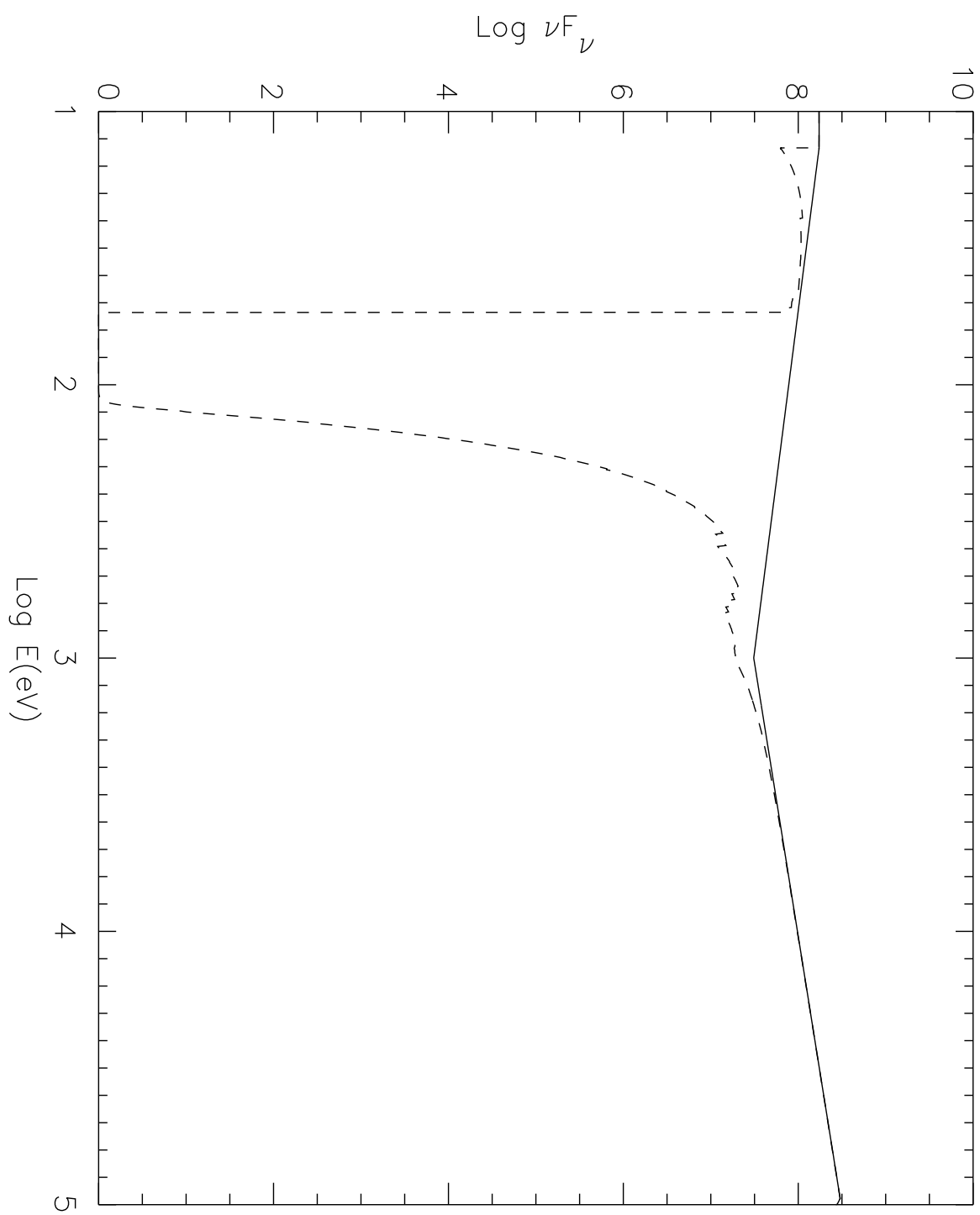


Fig. 5b.

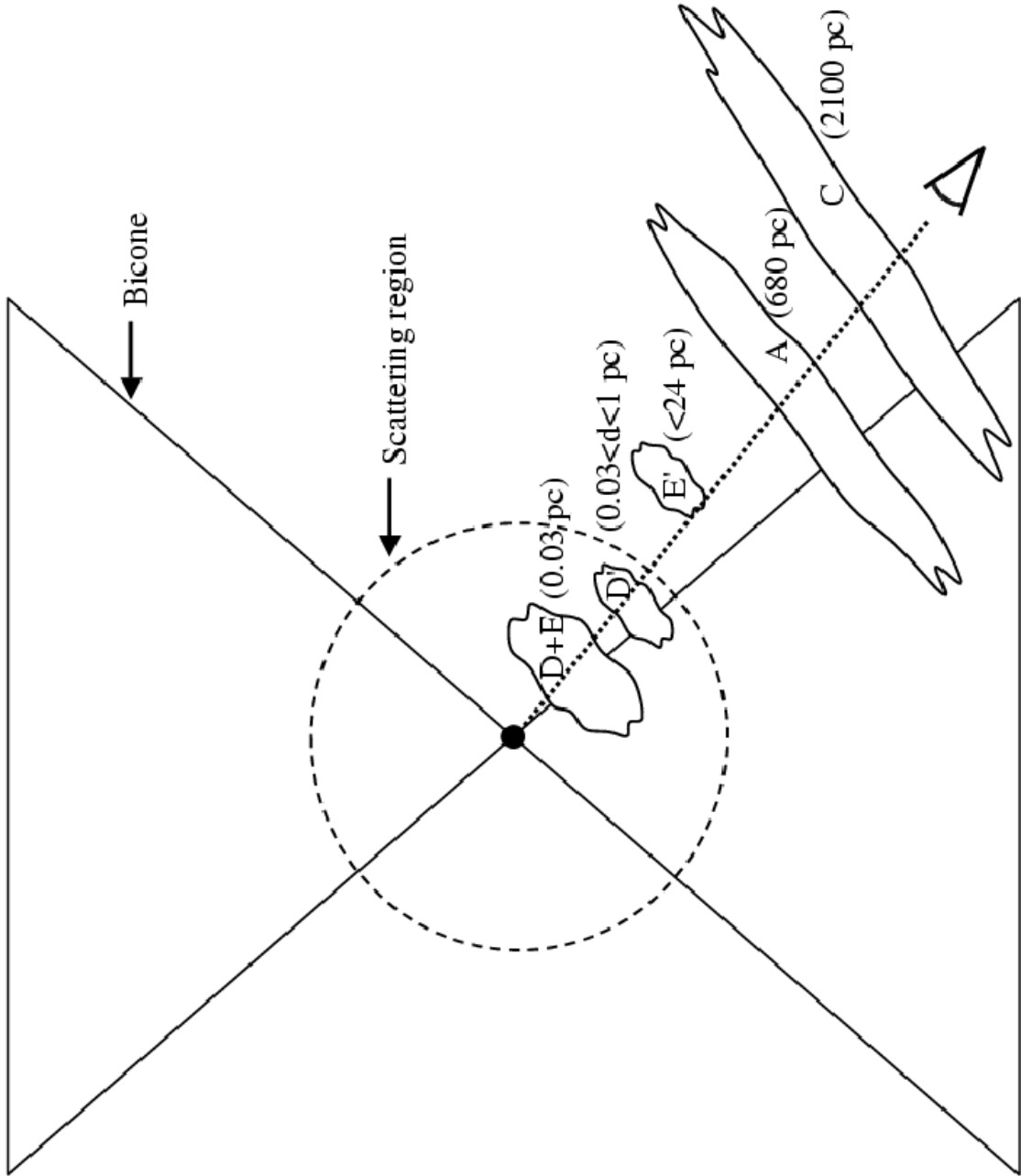


Fig. 6.

TABLE 8
 PREDICTED IONIC COLUMN DENSITIES (cm^{-2}) FROM X-RAY ABSORBER MODEL^a

Element	I X	II XI	III XII	IV XIII	V XIV	VI XV	VII XVI	VIII XVII	IX XVIII
H	9.5E+16	4.0E+22							
He	3.2E+14	6.6E+19	3.9E+21						
C		1.0E+12	5.1E+15	4.0E+17	6.1E+18	5.3E+18	1.8E+18		
N		1.5E+11	1.5E+15	1.1E+17	1.9E+17	3.2E+18	1.2E+18	1.6E+17	
O		4.9E+12	7.2E+16	5.6E+17	7.5E+17	3.5E+18	1.9E+19	2.7E+18	2.0E+17
Ne		4.1E+12	3.6E+16	3.2E+16	1.8E+17	1.1E+18	8.5E+17	8.9E+17	1.3E+18
	9.9E+16	2.7E+15							
Mg		6.2E+11	2.8E+15	2.9E+15	2.8E+15	1.8E+16	9.7E+16	3.1E+17	4.9E+17
	2.8E+17	1.1E+17	3.9E+15	4.7E+13					
Al		2.6E+11	1.7E+14	1.7E+14	1.1E+15	7.1E+15	2.3E+16	3.8E+16	3.3E+16
	1.2E+16	3.3E+15	8.6E+13	6.9E+11					
Si		1.7E+11	2.1E+13	1.5E+15	1.1E+16	6.4E+16	2.3E+17	3.7E+17	
	3.3E+17	1.8E+17	4.1E+16	9.6E+15	1.7E+14	8.7E+11			
P		1.3E+10	2.7E+12	1.9E+13	1.1E+14	8.0E+14	2.6E+15	4.4E+15	
	3.6E+15	2.3E+15	8.3E+14	1.9E+14	2.9E+13	3.6E+11			
S		4.3E+11	7.0E+13	8.4E+14	4.0E+15	2.6E+16	9.1E+16	1.6E+17	
	1.5E+17	1.1E+17	4.9E+16	1.2E+16	1.6E+15	2.4E+14	2.1E+12		
Fe		1.5E+10	3.0E+14	1.3E+15	3.8E+15	9.6E+15	3.9E+16	1.6E+17	
	2.4E+17	2.8E+17	3.2E+17	2.5E+17	1.6E+17	9.3E+16	2.6E+16	1.4E+16	1.3E+15
Ni		1.8E+12	2.1E+12	2.8E+13	1.6E+14	8.8E+14	4.9E+15		
	1.1E+16	1.86E+16	1.4E+16	1.1E+16	7.1E+15	3.8E+15	1.6E+15	5.3E+14	1.5E+14

^aU = 0.86, $N_{eff} = 4 \times 10^{22} \text{ cm}^{-2}$.